Boundary-Layer Meteorology (2006) 119: 195–238
DOI 10.1007/s10546-005-9024-6

A CASE STUDY ON THE EFFECTS OF HETEROGENEOUS SOIL MOISTURE ON MESOSCALE BOUNDARY-LAYER STRUCTURE IN THE SOUTHERN GREAT PLAINS, U.S.A. PART I: SIMPLE PROGNOSTIC MODEL

ANKUR R. DESAI[1,*], KENNETH J. DAVIS[1], CHRISTOPH J. SENFF[2], SYED ISMAIL[3], EDWARD V. BROWELL[3], DAVID R. STAUFFER[1] and BRIAN P. REEN[1]

[1]*Department of Meteorology, The Pennsylvania State University, 503 Walker Building, University Park, PA 16802, U.S.A.;* [2]*Atmospheric Lidar Division, NOAA Environmental Technology Laboratory, Boulder, CO, U.S.A.;* [3]*Atmospheric Sciences Division, NASA Langley Research Center, Hampton, VA, U.S.A.*

(Received in final form 15 August 2005 / Published online: 17 December 2005)

Abstract. The atmospheric boundary-layer (ABL) depth was observed by airborne lidar and balloon soundings during the Southern Great Plains 1997 field study (SGP97). This paper is Part I of a two-part case study examining the relationship of surface heterogeneity to observed ABL structure. Part I focuses on observations. During two days (12–13 July 1997) following rain, midday convective ABL depth varied by as much as 1.5 km across 400 km, even with moderate winds. Variability in ABL depth was driven primarily by the spatial variation in surface buoyancy flux as measured from short towers and aircraft within the SGP97 domain. Strong correlation was found between time-integrated buoyancy flux and airborne remotely sensed surface soil moisture for the two case-study days, but only a weak correlation was found between surface energy fluxes and vegetation greenness as measured by satellite. A simple prognostic one-dimensional ABL model was applied to test to what extent the soil moisture spatial heterogeneity explained the variation in north–south ABL depth across the SGP97 domain. The model was able to better predict mean ABL depth and variations on horizontal scales of approximately 100 km using observed soil moisture instead of constant soil moisture. Subsidence, advection, convergence/divergence and spatial variability of temperature inversion strength also contributed to ABL depth variations. In Part II, assimilation of high-resolution soil moisture into a three-dimensional mesoscale model (MM5) is discussed and shown to improve predictions of ABL structure. These results have implications for ABL models and the influence of soil moisture on mesoscale meteorology.

Keywords: Boundary-layer depth, Convective boundary layer, Lidar, Soil moisture, Surface buoyancy flux.

* E-mail: adesai@psu.edu

1. Introduction

Spatial and temporal evolution in the depth of mixing in the atmospheric boundary layer (ABL) can have a profound influence on local weather and cloud cover. The causes of mesoscale (tens to hundreds of km) variations in the ABL depth are not well understood but have been shown to be mediated by surface heterogeneity (Mahrt, 2000). We present a case study of observed mesoscale ABL variations on 12 and 13 July 1997 across the Southern Great Plains region of Oklahoma and Kansas, U.S.A. Balloon sounding and lidar observed ABL depth varied by as much as 1.5 km across 400 km on 12 July but only varied less than 0.5 km on 13 July. Both days had clear to partly-cloudy weather following rain on 10–11 July and midday ABL wind speeds of 7–10 m s^{-1} (Table I).

The observed variations in mesoscale ABL depth cannot be explained by larger scale boundaries such as fronts or drylines since none were evident on the two anticyclonic dominated days. Previous work in the Southern Great Plains has shown that ABL depth as examined from balloon soundings varied by a factor of 3 and was driven mostly by variability in surface energy fluxes (Hubbe et al., 1997). Thus, we hypothesized that mesoscale ABL depth variability on the two case study days was also driven by the variability in surface energy fluxes.

Surface energy fluxes measured from short towers can be highly variable across the landscape since they are a function of local vegetation, soil type, soil moisture, micrometeorological processes and fetch. However, mesoscale spatial patterns in surface energy fluxes observed from many towers are indicative of mesoscale variations in surface properties or meteorology. Variability in surface energy flux has an impact on cloud cover, convective initiation, rainfall intensity and atmospheric stability (Yan and Anthes, 1988; Avissar and Pielke, 1989; Zhong and Doran, 1997; Avissar and Schmidt, 1998). Vegetation cover and surface water availability appear to be primary factors that explain large-scale patterns in surface fluxes, especially in sparsely vegetated areas (Dirmeyer et al., 2000; Betts, 2004), and variations in surface parameters and surface fluxes have been shown to generate mesoscale boundary-layer circulations (Segal and Arritt, 1992; Weaver, 2004). Climate models suggest that the Southern Great Plains is a region where soil moisture is strongly coupled to precipitation patterns (Koster et al., 2004) and ABL structure (Betts and Ball, 1996). Thus, we hypothesize that surface soil moisture can explain the mesoscale variability in surface energy flux, and consequently, ABL depth, since 12 and 13 July were preceded by rain on July 10 and 11.

These hypotheses are not necessarily new or surprising. But while theoretical and modelling work on surface flux and ABL evolution has been done, observational studies at this scale and with a large matrix of instruments

TABLE I

Weather conditions during the case study at the ARM-CART Central Facility.

Date	Mean temp. at 2 m (°C)	Max. temp. (°C)	Min. temp. (°C)	Pressure (hPa)	Precip (mm)	Water vapour mixing ratio ($g\,kg^{-1}$)	Wind speed at 10 m ($m\,s^{-1}$)	Wind direction (degrees)
10 July 97	26	33	22	977	9	16.1	6	155
11 July 97	25	31	21	977	5	17.6	6.1	152
12 July 97	28	34	23	977	0	16.4	8.1	168
13 July 97	29	36	23	975	0	16.2	7.2	173

are uncommon. High spatial resolution and frequent temporal observations of ABL depth, surface energy fluxes, soil moisture, and surface vegetative properties are rare and not a part of routine observations. The Southern Great Plains 1997 (SGP97) hydrology experiment (Jackson, 1997) was one of few studies that included a large array of observations to allow for an examination of the causes of mesoscale ABL depth variability.

The objective of this study was to examine the causes of spatial variability in ABL development across the SGP97 area and to test new tools for studying this variability. To accomplish this objective, we explore the relationship between two land-cover variables and surface energy flux and develop a simple ABL model to examine the impact of surface forcing heterogeneity on ABL depth. We have chosen to use an empirical model tuned to the region and time period in order to maximize the combination of spatial resolution and areal coverage, and to test a unique remote sensing data source.

The two surface remote sensing instruments used in this study are the U.S. National Oceanic and Atmospheric Administration (NOAA) Advanced Very High-Frequency Radiometer (AVHRR) and the Electronically Scanned Thinned Array Radiometer (ESTAR), and their two respective land-cover measurements are vegetation cover and surface soil moisture. ESTAR is a passive microwave-based remote sensing system (Le Vine et al., 1994) that was flown on the U.S. National Aeronautics and Space Administration (NASA) P-3 aircraft across the SGP97 study area for several days to validate ESTAR operation and soil moisture retrieval algorithms (Jackson et al., 1999). Along with ESTAR, NASA Langley's Lidar Atmospheric Sensing Experiment (LASE) was flown on the P-3 to measure high vertical resolution aerosol scattering ratio and water vapour profiles using the Differential Absorption Lidar (DIAL) technique (Browell et al., 1997). High-resolution ABL depth measurements were derived from the LASE data.

The primary questions we asked in this study were: (1) Was there any correlation between the observed mesoscale ABL depth spatial variability and surface energy flux variability? (2) Was there any correlation between mesoscale surface flux variability and surface parameters? and (3) At what scale did surface parameters appear to influence ABL depth variability? In this study, we examined observed ABL depth from balloon soundings and airplane-mounted lidar during the drying period. We compared these depths to observations of integrated surface buoyancy flux measured at surface energy flux stations. We also compared energy fluxes to remotely-sensed measurements of soil moisture and vegetation. A simple one-dimensional (1-D) ABL model was developed and applied to further understand to what extent and scale did surface properties explain observed ABL depth. Part II of this study examines the influence of assimilating high resolution soil moisture into a full three-dimensional (3-D) mesoscale model (Reen et al., submitted).

2. Case Study Description

2.1. Southern great plains 1997 study

The Southern Great Plains 1997 field study occurred during late spring and summer of 1997 over northern Oklahoma and southern Kansas, U.S.A. (Figure 1). The area can be characterized as sub-humid grasslands with flat to moderately rolling terrain and a maximum relief of less than 200 m. Grassland and winter wheat are the dominant land-use types (Jackson et al., 1999). Local standard time (LST) is UTC – 6 hours.

The primary goal of SGP97 was validation of the soil moisture retrieval algorithms of ESTAR, which has been previously shown with *in-situ* data by Jackson et al. (1999) and also by comparison with a mesoscale model driven with an offline land-surface model (Reen et al., submitted). An additional objective was to examine the effect of soil moisture on the evolution of the ABL and clouds over the Southern Great Plains. In addition to the LASE and ESTAR, data were also collected by the U.S. Department of Energy (DOE) Atmospheric Radiation Measurement Cloud and Radiation Testbed (ARM-CART) flux and balloon sounding facilities, Oklahoma Mesonet weather stations, two aircraft equipped to measure surface energy fluxes and SGP97 flux towers set up by the U.S. Department of Agriculture Agricultural Research Service (USDA ARS), University of Wisconsin – Madison, the NASA Jet Propulsion Laboratory, Georgia Tech, NOAA Atmospheric Turbulence and Diffusion Division (ATDD) and the University of Arizona. ESTAR and LASE observations from 12 to 13 July are central to this study. Additional site information and data access are available at http://www.arm.gov/sites/sgp.stm, http://disc.gsfc.nasa.gov/fieldexp/SGP97/, and http://hydrolab.arsusda.gov/sgp97.

2.2. Case study conditions

Conditions prior and during the case study observed at the ARM-CART Central Facility Surface Meteorological Observation System consisted of warm, moist conditions with moderate southerly and south-easterly winds (Table I). Precipitation fell from 8 July through 11 July, primarily on 10 July (MacPherson, 1998). There was a strong north–south precipitation gradient across the measurement domain as observed by precipitation measurement sites included in the Global Energy and Water Cycle Experiment (GEWEX) daily precipitation composite (Figure 2). Total precipitation from 8 to 12 July, averaged across 1 degree latitude bands within the roughly 400 km SGP97 domain, varied from less than 5 mm in the south to greater than 50 mm in the north. This variability in antecedent

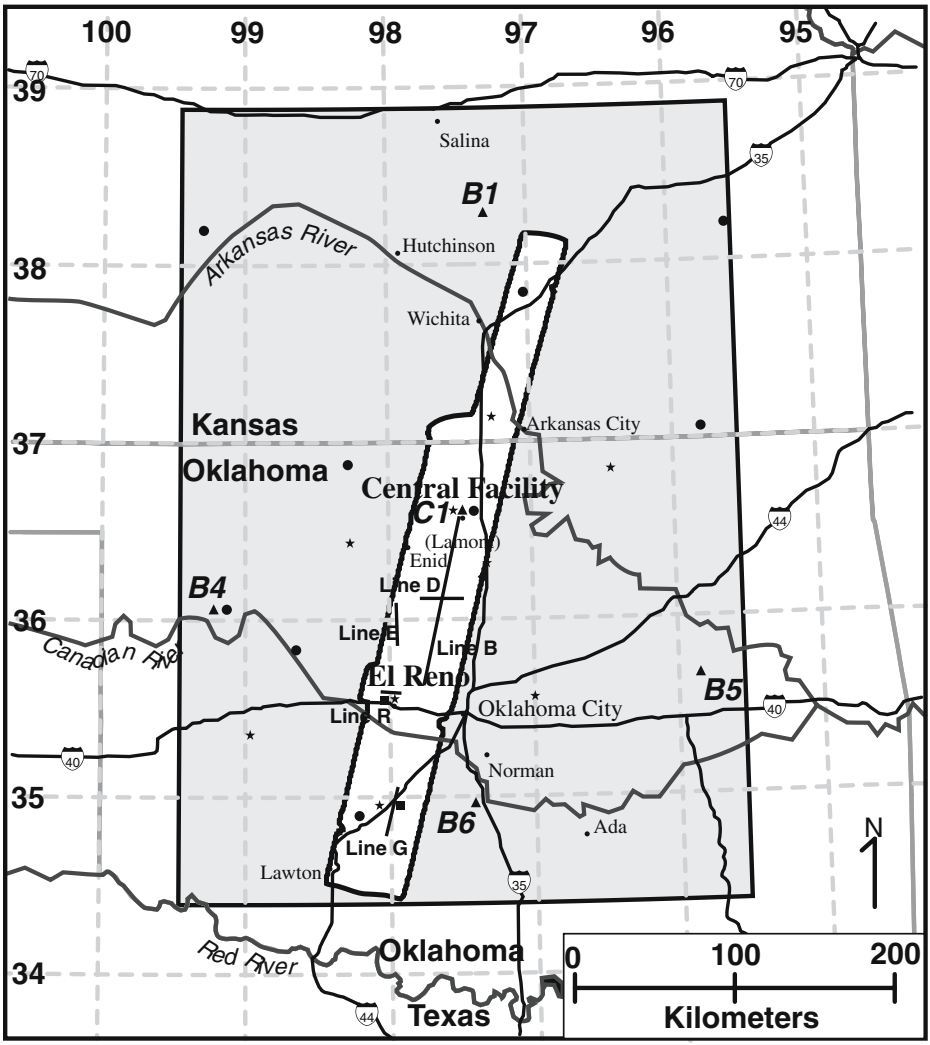

Figure 1. Map of Southern Great Plains 1997 study area and measurement site locations. NDVI (grey box) and ESTAR (white box) coverage on 12 July is also noted.

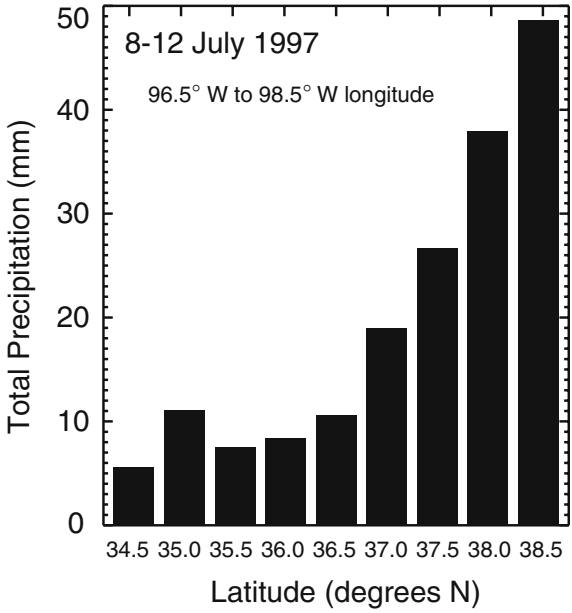

Figure 2. Observed total precipitation from 8 to 12 July 1997 averaged across 1 degree latitude bands centred on the latitudes shown and with longitude ranging from 96.5° W to 98.5° W.

precipitation was the primary cause in observed variation in surface soil moisture on 12 and 13 July.

3. Observations

Our primary goal was to examine the spatial variability of ABL depth and relate it to variability in surface energy fluxes and surface parameters. Point-based estimates of ABL depth were based on ARM-CART balloon soundings. North–south tracks of observed ABL depth were derived from the LASE aerosol data. Remotely-sensed surface soil moisture, a remotely sensed vegetation index and a spatially distributed set of temporally continuous measurements of surface energy flux were used to correlate point-based flux measurements to spatial maps of soil moisture and vegetation cover. These data came respectively from airplane-mounted ESTAR, NOAA AVHRR, and various tower-based flux stations spread across the SGP97 area. Energy fluxes were also observed from aircraft in various parts of the SGP97 area. For SGP97, clear, sunny days and the availability of ESTAR, AVHRR, LASE and a full suite of flux data coincided on 12–13 July, during the drying period after prior rainfall.

3.1. Soundings

ARM-CART Balloon-Borne Sounding System (BBSS) balloon soundings were launched once every 3 hours from five locations during the study time frame (Table II and Figure 1). One balloon sounding was located wholly within the ESTAR region on both days. Balloon sounding output was used in this study to compute potential temperature profiles and visually estimate ABL depth from these profiles. Balloon sounding wind speed and direction were used for advection and subsidence calculations. Vertical resolution was approximately 10 m, and ABL depth was chosen visually to the nearest 25 m with $\pm$ 50 m accuracy. Additional information about the BBSS system is at http://www.arm.gov/instruments/instrument.php?id=6.

3.2. Lidar

The LASE system was developed at the NASA Langley Research Center to measure atmospheric water vapour profiles, aerosol profiles and cloud distributions from aircraft (Browell et al., 1997). LASE is a compact and highly engineered differential absorption lidar system that has demonstrated autonomous operation from the high-altitude ER-2 aircraft as a precursor to the development of a space-borne DIAL system. During SGP97, LASE was reconfigured and operated in the nadir mode from the NASA P-3 aircraft. The laser system consists of a double-pulsed Ti:sapphire laser that operates in the 815 nm absorption band of water vapour and is pumped by a frequency doubled Nd:YAG laser. The double pulsing is needed to generate the *on* and *off* line pair needed for the DIAL water vapour measurements (Browell, 1989). The *on* and *off* lines are spectrally positioned on the water vapour absorption line so that there is insignificant absorption at the *off* line and optimum absorption at the *on* line due to the presence of water vapour in the atmosphere.

Lidar measurements at the *off* line were used to derive aerosol backscattering profiles. The *off* line lidar signals were background subtracted and range corrected (by multiplying by the square of the range) to derive the relative atmospheric backscattering profiles. The relative backscattering profiles can be used to obtain ABL properties (Ismail et al., 1998). Aerosol backscatter profiles from the LASE were used to derive ABL depth variations with high spatial resolution (Davis et al., 2000). Resolution was 150 m in the horizontal and the vertical range gate was 30 m. ABL depth was computed using a stepped wavelet function with a 250-m dilation scale. Further details on LASE are available at http://asd-www.larc.nasa.gov/lidar/lidar.html and http://asd-www.larc.nasa.gov/lidar/sgp97/sgp97.html. This study focused on late morning and midday north–south P-3 tracks on 12 and 13 July.

TABLE II

ARM balloon-borne sounding systems in the SGP97 region.

Station	Region	Location	Latitude	Longitude	12 July	dT/dz (K km^{-1})	z_i 0830 LST (m)	z_i 1130 LST (m)	z_i 1430 LST (m)	13 July	$d\theta_v/dz$ (K km^{-1})	z_i 0830 LST (m)	z_i 1130 LST (m)	z_i 1430 LST (m)
B1	North	Hillsboro, KS	38°18′00"	97°18′00"		10.9	625	875	1225		14.0	475	700	1400
C1	Central	Lamont, OK	36°36′36"	97°29′24"		10.5	650	1100	1975		18.4	475	1125	975
B6	South	Purcell, OK	34°57′36"	97°25′12"		10.8			2175		13.0	550	1000	1825
B4	West	Vici, OK	36°04′12"	99°12′00"		12.4	350	675	800		16.2	450	650	1000
B5	East	Morris, OK	35°40′48"	95°51′00"		8.5	475	850	1075		12.4	450	975	925

$d\theta_v/dz$ is the increase in virtual potential temperature of early morning soundings (0530 LST) between 0 and 500 m.

3.3. ESTAR

ESTAR was designed as a passive microwave remote sensor to be used in space for global soil moisture mapping at relatively coarse resolutions (10–30 km) (Le Vine et al., 1994). Surface (< 50 mm) soil moisture has been shown to be related to passive microwave brightness temperature (USDA ARS, cited 1997: Southern Great Plains 1997 hydrology experiment plan [Available online at http://hydrolab.arsusda.gov/sgp97/explan/]). During SGP97, ESTAR was operated at a nominal altitude of 7.5 km from the NASA Wallops Flight Facilities' P-3B aircraft.

Information from ESTAR was gridded to produce a map of microwave ground reflectance across and along the airplane track at 400-m resolution. Soil moisture from ESTAR was computed from this brightness temperature map and the Fresnel reflectance inverse model equation for horizontal polarization (Jackson et al., 1999). Inputs to this model included microwave brightness temperature, soil temperature, vegetation type, vegetation water content, surface roughness, soil bulk density and soil texture. Model inputs were derived from Oklahoma Mesonet weather stations and LandSat Thematic Mapper (TM) land-cover data. The output soil moisture map was gridded to 800-m resolution. The average error in soil moisture compared to Oklahoma Mesonet observed soil moisture was 3% (Jackson et al., 1999). More information and data are available at http://disc.gsfc.nasa.gov/fieldexp/SGP97/estar.html.

3.4. AVHRR

NOAA AVHRR satellites produce visible and infrared images of the Earth's surface at regular intervals at a 1.1-km resolution in the green, red and infrared bands. The Normalized Difference Vegetation Index (NDVI), a standard measure of vegetative cover, is calculated as the ratio of the difference over the sum of the visible red and near infrared bands (Avery and Berlin, 1992). AVHRR NDVI data for the SGP97 region were available in the morning, afternoon and evening of 12 July and the morning and afternoon of 13 July. In this study, afternoon NDVI data were used from the NOAA-12 satellite.

In general, NDVI values range from -1 to 1, with typical NDVI values for vegetated areas around 0.6, and only marginal increases in NDVI with increasing vegetation cover after that threshold (Gillies and Carlson, 1995). NDVI is often used as a proxy measure for leaf area index (LAI) (Chehbouni et al., 1997).

3.5. Surface fluxes

Surface fluxes of latent and sensible heat were measured at numerous sites across the SGP97 domain by DOE ARM-CART and other investigators (Table III), sites being chosen for representative vegetation of the region and availability/quality of data. Both Bowen ratio and eddy covariance systems were deployed during SGP97, with several stations also measuring soil heat flux and net incoming radiation. Details on ARM-CART eddy covariance instrumentation are at http://www.arm.gov/instruments/instrument.php?id=14 and in Hart et al. (1998). Details on ARM Bowen ratio systems can be found in Wesely et al. (1995) and at http://www.arm.gov/instruments/instrument.php?id=13. Individual investigator flux systems are described at http://disc.gsfc.nasa.gov/fieldexp/SGP97/srf_flux_teams.html.

A typical flux random measurement error of 10% was assumed in this study. Turbulent fluxes measured with eddy covariance systems are also implicated in the energy balance closure problem (Twine et al., 2000). Typically, the sum of the observed eddy covariance latent and sensible heat fluxes is smaller than the sum of net radiation and soil heat flux, due partly to errors in turbulent measurements and instrument sampling footprint variability (Twine et al., 2000). Since the magnitude of this error is unconstrained, closure issues were neglected in this study and flux stations were assumed to have underestimated surface energy fluxes by relatively similar amounts.

3.6. Flux aircraft

The Canadian National Research Council Twin Otter and the NOAA Long-EZ research aircraft each flew 27 missions to measure the surface and airborne energy fluxes across a number of lines (B, E, D, R and G in Figure 1) in the SGP97 domain (Dobosy and MacPherson, 1999). Leg lengths ranged from 14 to 108 km. These aircraft were instrumented to measure standard meteorological and radiometric variables, and fluxes of sensible and latent heat, momentum and CO_2.

Long-EZ fluxes were computed using single-pass low-level flight transects (30 m altitude for most legs, except 150 m over line G). Individual flux "fragments" were computed at 1-s (50 m) intervals from high-frequency data, and leg average fluxes were computed from the deviations of the high-pass filtered flux fragments using a 400-s (20 km) bandwidth to ensure contributions of larger-scale atmospheric motions to the flux (R. Dobosy, 2005, personal communication). For the Twin Otter, run length high-frequency linearly detrended time histories were used directly for computation of flux (J. MacPherson, 2005, personal communication). Good agreement

TABLE III
Location and site characteristics of flux towers used in this study.

Station	Location	Investigator	Latitude	Longitude	Surface Type
North					
E2	Hillsboro, KS	DOE[a]	38°18′22"	97°18′04"	Pasture
E6	Towanda, KS	DOE[a]	37°50′31"	97°01′12"	Alfalfa
E9	Ashton, KS	DOE[a]	37°07′59"	97°15′58"	Pasture
North Central (Central Facility)					
E14	Lamont, OK	DOE[a]	36°36′22"	97°29′06"	Pasture and wheat
E13	Lamont, OK	DOE[a]	36°36′18"	97°29′08"	Pasture and wheat
E15	Ringwood, OK	DOE[a]	36°25′52"	98°17′02"	Pasture
South Central (El Reno)					
ER01JPBK	El Reno, OK	JPBK[b]	35°33′22"	98°00′59"	Ungrazed grassland
ER01PS	El Reno, OK	PS[c]	35°33′22"	98°00′59"	Pasture
E19	El Reno, OK	DOE[a]	35°32′56"	98°01′12"	Ungrazed pasture
ER05JPBK	El Reno, OK	JPBK[b]	35°32′53"	98°02′09"	Grazed grassland
ER05PS	El Reno, OK	PS[c]	35°32′53"	98°02′09"	Winter wheat
ER13JPBK	El Reno, OK	JPBK[b]	35°32′24"	98°03′47"	Harvested winter wheat
South (Little Washita)					
LW02TM	Chickasha, OK	TM[d]	34°57′41"	97°58′20"	Pasture
E26	Cement, OK	DOE[a]	34°57′25"	98°04′34"	Pasture
West					
E1	Larned, KS	DOE[a]	38°12′07"	99°18′58"	Winter wheat
E8	Coldwater, KS	DOE[a]	37°19′59"	99°18′32"	Grazed pasture
E16	Vici, OK	DOE[a]	36°03′40"	99°08′02"	Winter wheat
East					
E7	Elk Falls, KS	DOE[a]	37°22′59"	96°10′48"	Pasture
E10	Tyro, KS	DOE[a]	37°04′05"	95°47′17"	Alfalfa
E20	Meeker, OK	DOE[a]	35°33′50"	96°17′17"	Pasture

[a]Department of Energy, Atmospheric Radiation Measurement program.
[b]John Preuger, Bill Kustas, USDA ARS.
[c]Patrick Starks, USDA ARS.
[d]Tilden Meyers, NOAA ARL ATDD.

was found among Long-EZ, Twin Otter and tower measured fluxes during concurrent passes on prior SGP97 missions (R. Dobosy, 2005, personal communication).

Line average fluxes were used in this case study. Shorter line fragments were not studied due to issues related to inherent turbulent sampling variability with aircraft measured fluxes (LeMone et al., 2003). Flux uncertainty was estimated to be approximately 20% (Mann and Lenschow, 1994). More information on these flights and flux processing details can be found at http://disc.gsfc.nasa.gov/fieldexp/SGP97/air_boundary.html.

4. Methods

4.1. Surface parameters and correlations to buoyancy flux

Surface energy fluxes observed from short towers and aircraft were examined for spatial correlation with surface parameters and ABL depth. Since our goal was to examine the effect of total surface forcing on midday ABL depth, and since observed latent heat fluxes were larger than sensible heat fluxes on both days, we examined time integrated surface buoyancy flux from morning (0530 LST) to afternoon (1230 LST):

$$F = \int_{t_0}^{t_1} \left(\overline{w'\theta_v'}\right)_s dt, \tag{1}$$

where surface buoyancy flux ($\mathrm{K\,m\,s^{-1}}$) was calculated from observed surface energy fluxes as

$$\overline{w'\theta_v'} = \frac{H}{\rho c_p} + 0.61\overline{\theta}\left(\frac{L}{\rho_d L_v}\right) \tag{2}$$

and where H is sensible heat flux ($\mathrm{W\,m^{-2}}$) and L is latent heat flux ($\mathrm{W\,m^{-2}}$).

The construction of a quantitative relation between remotely sensed vegetation greenness or soil moisture to surface buoyancy flux required registration of point locations of flux towers to the gridded surface parameter data. Since fluxes measured from small towers (<10 m high) tend to have a footprints that extend about 100–2000 m upwind (Pelgrum and Bastiaanssen, 1996), we averaged surface parameters for two pixels (1.6 km for ESTAR and 2.2 km for AVHRR) in the upwind direction for each site. Errors arising from the misalignment of station coordinates onto the surface parameter grids were considered by calculating a 3×3 pixel standard deviation of the surface parameter for each station coordinate and including this as an error to the assigned value of the surface parameter for that station.

Time integrated buoyancy flux from 0530 to 1230 LST was compared to soil moisture and vegetation cover, and linear correlations were created between surface parameters and total forcing for both 12 and 13 July and for ESTAR soil moisture and AVHRR NDVI. Regression was performed using the Fitexy algorithm (information at: http://idlastro.gsfc.nasa.gov/ftp/pro/math/fitexy.pro), a linear least squares regression method that can account for errors both in the surface parameter (due to instrument validation and misalignment error) and surface forcing (10% uncertainty). The fits were modified at the tails to prevent the net forcing from exceeding mean observed total available energy (net radiation − soil heat flux) and from falling below the lowest observed surface buoyancy flux.

We tested the reliability of a strong fit found between soil moisture and F by comparing soil moisture modelled buoyancy flux to airplane observed leg average flux. Soil moisture values along airplane legs were extracted from ESTAR soil moisture pixels 5 km upwind of the leg to account for flux footprint and advection as recommended by Song and Wesely (2003). Time varying modelled surface buoyancy flux was computed using a sinusoidal model:

$$\left(\overline{w'\theta'_v}\right)_s = \frac{(\frac{\pi}{2})F}{3600\,(t_1 - t_0)} \sin\left(\frac{\frac{\pi}{2}\,(t - t_0)}{t_1 - t_0}\right), \tag{3}$$

where t is time in hours, F is modelled from the relationship between ESTAR soil moisture and observed tower-based surface fluxes, and t_0 and t_1 are the limits of integration in Equation (1).

4.2. ABL model

The correlation of soil moisture to surface buoyancy flux, soil moisture transects derived from ESTAR, early morning virtual potential temperature profiles, and an ABL model were used to model ABL depth along the north–south P-3 track. A model for convective boundary-layer growth in response to heterogeneous surface forcing was developed by Gryning and Batchvarova (1996) based on the encroachment models derived in Batchvarova and Gryning (1991), Carson (1973) and Tennekes (1973):

$$\left\{\frac{z_i^2}{(1+2A)z_i - 2B\kappa L} + \frac{Cu_*^2 T}{\gamma g(1+A)z_i - B\kappa L}\right\}\left(\frac{\partial z_i}{\partial t} + u\frac{\partial z_i}{\partial x} + v\frac{\partial z_i}{\partial y} - w_s\right) = \frac{\left(\overline{w'\theta'_v}\right)_s}{\gamma}, \tag{4}$$

where z_i is mixed-layer depth, κ is the von Kármán constant (0.4), L is the Obhukhov length, u_* is friction velocity, u and v are the along-track

and across-track mean mixed-layer wind speed components, w_s is subsidence rate, T is near-surface air temperature, g is gravity, γ is the virtual potential temperature gradient above z_i, and A, B and C are parameterization constants.

Batchvarova and Gryning (1991) show that terms related to mechanical turbulence and 'spin-up' are only important when the mixed-layer depth is small (e.g., early morning). Since our goal was to evaluate midday mixed-layer depth variability, and observed sounding data showed minimal variation of z_i in the morning, we neglect these terms and instead initialize the model at mid-morning (0830 LST) with constant z_i. Additionally, since we were attempting to model observed ABL depth across the north–south P-3 track and the wind direction on both days was nearly parallel to the track, we neglect across-track advection and instead average soil moisture data for 15 km (1 m s^{-1} for 4-hour model period) upwind in the crosswind direction as a proxy for across-track advection. Equation (4) can then be simplified and rearranged to

$$\frac{\partial z_i}{\partial t} = \underbrace{\frac{(1+2A)\left(\overline{w'\theta_v'}\right)_s}{z_i\gamma}}_{\text{(a)}} \underbrace{-\frac{\partial u z_i}{\partial x}}_{\text{(b)}} + \underbrace{w_s}_{\text{(c)}}, \tag{5}$$

where A is typically assumed to be 0.2 (Tennekes, 1973) and u and x are in the direction of the P-3 track. Unlike Equation (4), we have also included in term b of Equation (5) the effect of convergence/divergence on ABL depth due to the spatial variation in wind velocity.

This simple model treats the convective boundary layer as a shallow well-mixed 1-D fluid moving with the mean wind. ABL growth in this model is controlled by three terms: (a) a local forcing that encroaches upon the mixed-layer inversion above z_i, (b) a combined z_i advection and local-scale convergence/divergence term, and (c) a net large-scale lifting/subsidence term. Entrainment flux at the top of the ABL is parameterized as a constant fraction of surface buoyancy flux; shear-driven mixing, cross-track advection, and boundary-layer dynamics are ignored. These effects are better simulated with a 3-D mesoscale model, whose application is discussed in Part II of this paper (Reen et al., submitted). The modelling approach used here is admittedly simplistic, but provides an easy way to model and analyze ABL depth using solely observed data in the region and a minimal number of assumptions.

We numerically solved Equation (5) along the north–south 413 km P-3 track on 12 July and the 286 km P-3 track on 13 July with 1000 m horizontal resolution and a 30-s time step. The model was run from 0830 to 1230 LST, and the 0830 LST initial ABL depth was set to a constant value along the track based on balloon soundings near the track (650 m on 12

July and 500 m on 13 July). The equation was numerically solved at each grid point and time step using a second-order Lax-Wendroff explicit differential scheme (Garcia, 2000). Each model run required 2–5 minutes of computation time on a standard desktop computer.

Time and space varying surface buoyancy flux was estimated using the regression of F to ESTAR soil moisture and Equation (3). Soil moisture to the north and south of the ESTAR domain was assumed to be constant and equal to the northernmost or southernmost observed soil moisture values, respectively. Along-track wind speeds (u) were calculated by interpolation (inverse distance) of balloon sounding along-track wind speeds. Temperature gradient at the mixed-layer height was also calculated by spatial interpolation of early morning (0530 LST) virtual potential temperature balloon soundings at $z_i - 50$ m and $z_i + 50$ m at each grid point and time step. Large-scale subsidence velocity was assumed to be constant over the track but allowed to vary with time and computed using the continuity equation and balloon sounding profiles of wind speed:

$$w_s = \int_{sfc}^{h} \left(\frac{\partial u}{\partial x} + \frac{\partial v}{\partial y} \right) dz. \tag{6}$$

Modelled ABL depth was extracted along the time and space varying last two north–south P-3 tracks on each day: 1118–1200 LST (hereafter referred to as 1130 LST) and 1207–1231 LST (1215 LST) on 12 July, and 1038–1105 LST (1045 LST) and 1110–1200 LST (1130 LST) on 13 July.

To separate the effects of spatial variability in initial temperature profiles from variability in surface fluxes on ABL development, we also ran this model using only one of three soundings near the P-3 track (B6-south, C1-central, B1-north) to compute γ for all pixels instead of interpolating all five soundings. Additional model runs to test the effect of model terms on ABL depth were performed for cases of, (1) constant surface forcing, (2) constant wind speed, and (3) no advection, convergence or subsidence. Scales of ABL depth and surface parameter covariance were examined by running the model with soil moisture averaged for every 2, 4, 8, 16, 32, 128 or 256 km and linearly resampled to the 1-km grid.

5. Results

5.1. Observed ABL depth

5.1.1. *Balloon Soundings*

Balloon soundings were available to examine daytime ABL depth growth at 0830 (mid-morning), 1130 (midday) and 1430 (afternoon) LST (Table II). Potential temperature profiles showed a north–south gradient in ABL

depth on 12 July by afternoon, especially along the central longitude of the domain (sites B1-north, C1-central and B6-south; Figure 1). At all times, depths were generally higher in the south and central region than the north on 12 July. At midday, highest depths (1100 m) were seen in the central sounding, although southern soundings were missing at this time. By afternoon, the southern part of the domain had the highest depths (2175 m). East and west of the central longitude (B5 and B4) had less rapid growth and consequently a lower ABL depth by afternoon, though the eastern ABL depth was consistently higher than the west, due to the weaker inversion strength. Even though the inversion strength was weaker in the east than the central region, the ABL depth was lower due to a lower surface buoyancy flux (Table IV).

Excluding the east and west soundings, afternoon ABL depths on 13 July were on average 425 m shallower than 12 July, but a similar pattern remained. At midday, low depths were seen in the north (700 m), moderate in the south (1000 m) and relatively high in the centre (1125 m). By afternoon, the highest depths were in the south (1825 m). However, the ABL had also grown rapidly in the north (B1). The western sounding ABL depth in mid-morning and midday was similar to 12 July, but 125 m higher by afternoon compared to 12 July. The eastern sounding also had similar depths in mid-morning and midday, but the ABL was shallower by about 325 m in the afternoon compared to 12 July. Virtual potential temperature morning inversion strength was considerably greater on 13 July compared to 12 July, thus suppressing ABL growth in the early and mid morning.

5.1.2. *Lidar*

The spatial variations in ABL growth seen in the soundings along the central longitude of the domain were reflected in the LASE observed north–south ABL depths (Figure 3). LASE-derived ABL depths on 12 July by 1130 LST reached approximately 900 m above ground in the northern region ($> 37.25^\circ$ N) of the study domain and 2500 m above ground at the southern region (Little Washita area, $<35^\circ$ N) by 1115 LST. Low depths (900 m) were observed in the south-central region (El Reno area, 35–36.25° N) and the far northern part of the domain, and moderate depths (1,200 m) were observed in the north central region (Central Facility area, 36.25–37.25° N).

LASE observed depths were consistent with those observed by balloon soundings in the midday and afternoon, although central region depths were shallower than the midday central sounding (Table II). The mean ABL depth on 12 July across the 1130 LST track was 1233 m ± 443 m. This depth was higher than the mean midday ABL depth observed from the soundings (988 m) covering that region. The southern end of the domain had the most rapid ABL growth rate ($>1{,}200\ \mathrm{m\,h^{-1}}$) between 1015 and 1130 LST, but very little growth after that. The ABL in the south

TABLE IV

Flux tower data for 12 and 13 July 1997: sensible heat flux (H), latent heat flux (LE), net radiation (R_{net}), soil heat flux (G), integrated buoyancy flux from 0530 to 1200 LST ($\text{Int}_{\overline{w'\theta_v'}}$), ESTAR soil moisture (soil M) and AVHRR NDVI (NDVI).

Station	Type	H 1130–1230 LST (W m^{-2})	LE 1130–1230 LST (W m^{-2})	R_{net} 1130–1230 LST (W m^{-2})	G 1130–1230 LST (W m^{-2})	$\text{Int}_{\overline{w'\theta_v'}}$ 0530-1200 LST (K m)	Soil M (%)	NDVI
12 July								
North								
E2	BR	127	474	659	58	1800		0.32
E6	EC	72	353			800	31	0.44
E9	BR	91	461	611	59	1300	29	0.24
North Central (Central Facility)								
E14	EC	129	384			1800	28	0.15
E13	BR	236	350	645	59	3000	28	0.15
E15	BR	269	263	602	69	3000		0.45
South Central (El Reno)								
ER01JPBK	EC	104	386	742	73	1600	27	0.36
ER01PS2	BR	89	547	702	66	1800	27	0.36
E19	BR	92	536	669	41	1400	28	0.39
ER05JPBK	EC	123	391	685	55	1800	25	0.44
ER05PS	BR	166	355	715	55	2400	25	0.44
ER13JPBK	EC	278	121	643	140	3100	15	0.45
South (Little Washita)								
LW02TM	EC	157	306	690	78	2600	22	0.51
E26	BR	248	305	651	98	3100	18	0.51
West								
E1	EC	200	287			2100		0.43
E8	BR	137	81	291	73	1700		0.26
E16	EC	358	120			3200		0.44
East								
E7	BR	52	377	496	67	900		0.54
E10	EC	15	532			400		0.49
E20	BR	85	344	604	175	100		0.52
Mean		151	349	627	78	1900	26	0.39

TABLE IV
Continued.

Station	Type	H 1130–1230 LST ($W m^{-2}$)	LE 1130–1230 LST ($W m^{-2}$)	R_{net} 1130–1230 LST ($W m^{-2}$)	G 1130–1230 LST ($W m^{-2}$)	$Int_{\overline{w'\theta_v'}}$ 0530-1200 LST (K m)	Soil M (%)	NDVI
13 July								
North								
E2	BR	80	513	654	61	1200		0.45
E6	EC	66	324			900		0.35
E9	BR	52	493	606	61	1200		0.39
North Central (Central Facility)								
E14	EC	110	408			1600	21	0.29
E13	BR	203	380	638	54	2700	21	0.29
E15	BR	250	258	584	77	2800		0.24
South Central (El Reno)								
ER01JPBK	EC	72	407	735	77	1300	22	0.48
ER01PS2	BR	61	572	699	67	1400	22	0.48
E19	BR	50	572	664	42	1400	23	0.44
ER05JPBK	EC	87	406	681	52	1500	20	0.47
ER05PS	BR	134	389	712	52	2000	20	0.47
ER13JPBK	EC	345	118	633	138	3800	11	0.49
South (Little Washita)								
LW02TM	EC	153	320	683	97	2600	17	0.49
E26	BR	245	298	646	103	3200	13	0.46
West								
E1	EC	21	304			1100		0.32
E8	BR	134	84	286	68	1700		0.35
E16	EC	389	59			3700		0.40
East								
E7	BR	87	435	618	96	1500		0.56
E10	EC	26	490			400		0.59
E20	BR	93	333	606	180	300		0.49
Mean		133	358	630	82	1800	19	0.42

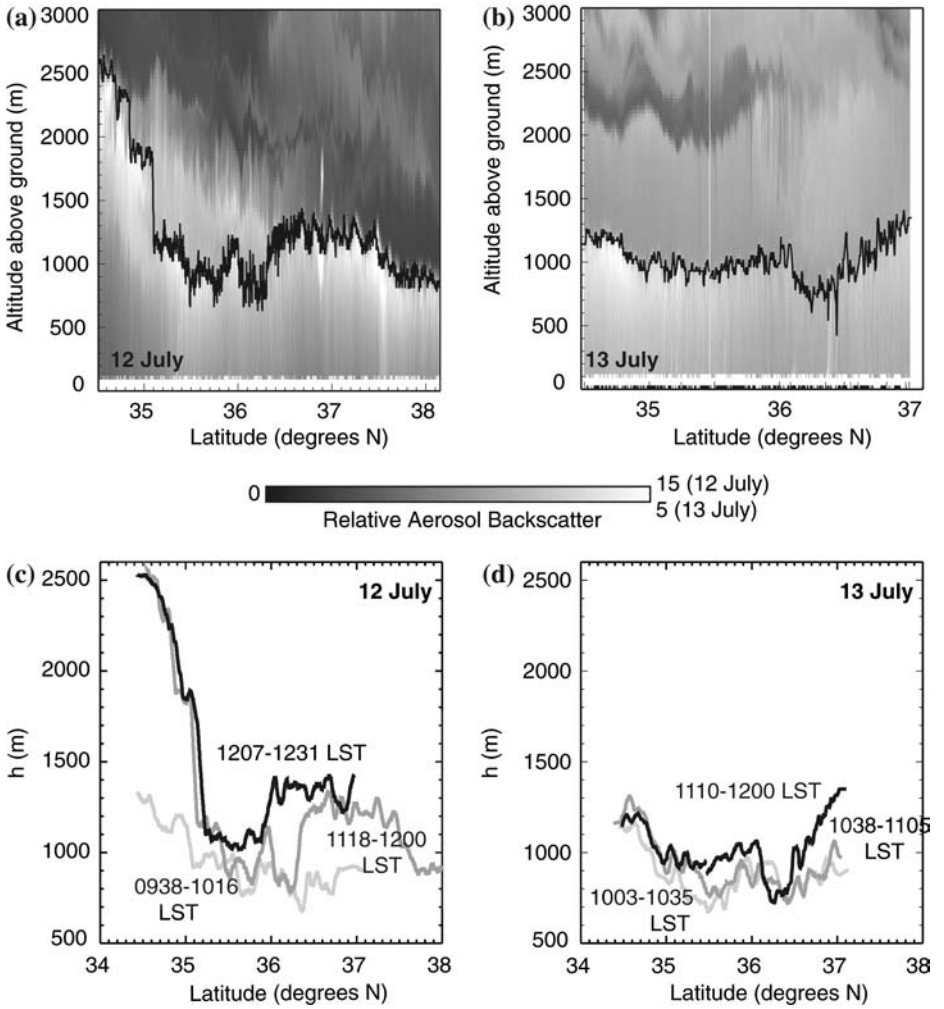

Figure 3. Image of a portion of the LASE flight track showing LASE relative aerosol backscatter and ABL depth (black line) over the 1130 LST tracks (a) 12 July and (b) 13 July. Smoothed LASE ABL depth from south to north (along the centre spine of the ESTAR domain) for late morning and midday legs on (c) 12 July and (d) 13 July.

central region was shallow and slow growing (<1000 m, <150 m h^{-1}), while the ABL in the north central region grew faster to reach a depth of approximately 1400 m. The rapid ABL deepening (approximately 500 m h^{-1}) in the north central region occurred earlier in the northern subsection (36.5–37° N) than the southern subsection (36–36.5° N).

Midday ABL depths on 13 July at 1130 LST were overall lower (mean 1006 m ± 141 m) especially at the southern end (Figure 3). ABL depth in the late morning was highest in the south (1000 m) and central (900 m), but by midday, ABL depths at the northern end matched the southern end

(1200–1300 m). This shift in ABL depth pattern is also seen in balloon soundings, but at a later time between the midday and afternoon soundings (Table II). Average sounding midday depth over the P-3 track was slightly lower (941 m) than LASE. Growth rates from 1015 to 1230 LST were highest (200 m h^{-1}) in the north, consistent with what was observed in the midday and afternoon soundings. In contrast to the soundings, very little ABL deepening was observed along the southern end of the track, with some slow growth (approximately 150 m h^{-1}) in the south central region. ABL depths appear to even have declined by 200 m from 1045 LST to 1200 LST near 36.25° N, similar to what was observed by the central area sounding, which showed a 150 m decrease in ABL depth from midday to afternoon.

5.2. Observed surface energy fluxes

Spatial variation in time-integrated surface buoyancy flux (Table IV) averaged by region reflected the variation seen in ABL depth on 12 July (Table II). Mean time-integrated surface buoyancy flux in the south, south-central, north-central and north regions was 2850, 2010, 2600, 1300 K m, respectively, similar in pattern to mean midday region-average sensible heat flux. Latent heat fluxes were largest in the south-central and north regions. These patterns were remarkably similar to the variation in midday ABL depth from south to north (high, low, moderately high, low). In contrast, a larger average time-integrated surface buoyancy flux was seen in the west (average, 2300 K m) compared to the east (average, 460 K m), opposite to the pattern of the midday ABL depth, which was slightly higher in the east (850 m east, 675 m west). It appears that the larger magnitude surface buoyancy flux in the west was unable to lead to a larger ABL depth there because the inversion strength was much higher in the west compared to all other sounding locations on 12 July (Table II),

Similar patterns in time-integrated surface buoyancy flux were observed on 13 July, though the total flux magnitude was slightly lower (Table IV). Region average time-integrated buoyancy flux was 2900, 1900, 2400, 1100 K m for the south, south-central, north-central and north regions, respectively, which were on average 7% smaller than 12 July. Midday sensible heat fluxes were smaller on 13 July, while latent heat fluxes were larger. Midday net radiation and soil heat flux were similar on both days. These variations are reflected in the sounding observed ABL depth in midday, but by afternoon the ABL grew in the northern region and declined the central region. LASE observed ABL depths also showed greater values to the north, despite the low surface buoyancy fluxes there. This may have been due to the larger variation in inversion strength from south to north on 13 July (Table II).

The east–west pattern of surface buoyancy flux on 13 July was similar to 12 July, but the region average time-integrated buoyancy flux declined by 5% in the west and increased by 59% in the east. Consequently, midday ABL depth was slightly lower to the west (650 m) compared to 12 July, and higher in the east (975 m), despite the greater inversion strength (Table II). However, by afternoon, ABL depths declined slightly in the east, and rose in the west.

Spatial variability in net radiation and soil heat fluxes was small, with net radiation slightly higher in the south compared to the north (Table IV). Surface energy fluxes had more station-to-station variability within the southern part of the domain than the northern part. Sensible heat flux averaged across all sites on both days peaked around 1130 LST at roughly $150\,W\,m^{-2}$, whereas latent heat flux peaked around 1300 LST at roughly $450\,W\,m^{-2}$. On both days, mean latent heat flux was greater than mean sensible heat flux for all times, high value consistent with net evaporation during the drying period.

Midday energy fluxes observed from aircraft showed greater buoyancy fluxes for transects in the south central region compared to the north central region line on 12 July (Table V). Buoyancy flux was larger on north central region lines on 13 July compared to 12 July, but soil was also drier. Line G in the southern region had very low sensible heat flux on 13 July, leading to low buoyancy flux even though soil was relatively dry. Line G latent heat fluxes were not similarly small. There is evidence that the low sensible heat flux may have been caused by radiative flux divergence and/or advection, given the higher altitude (150 m) flown on this line (R. Dobosy, 2005, personal communication). Correlation of soil moisture to aircraft buoyancy flux was larger than the correlation of NDVI to buoyancy flux.

5.3. Surface parameters and correlation to surface buoyancy flux

5.3.1. *Soil Moisture*

A strong north–south gradient was observed in soil moisture on both 12 July and 13 July (Figure 4). North–south line average soil moisture on 12 July depicted a gradient of dry soil (<20% soil volumetric water content) in the southern region, moderately dry (roughly 20%) with some small very dry patches (<10%) in the south-central and north-central regions, and a rapid increase around 36.5° N to moist soil, with soil moisture peaked near 40% at 37° N and levelled off to around 35% north of 37° N (Figure 5). The soil moisture pattern on 13 July was similar, but average soil moisture was lower ($13.8\% \pm 9.0\%$) compared to 12 July ($22.2\% \pm 6.5\%$). Primary variability in soil moisture corresponded well to the variability in

TABLE V

Long EZ and Twin Otter line-averaged fluxes for flight legs closest to 1200 LST, ESTAR line-averaged soil moisture and AVHRR NDVI for 12 and 13 July 1997.

Date	Line	Platform	Latitude	Longitude	Times (LST)	H ($W m^{-2}$)	LE ($W m^{-2}$)	$\overline{w'\theta_v'}$ ($K m s^{-1}$)	Avg. soil moisture (%)	NDVI
12 July										
North Central (Central Facility)										
	D	Long EZ	36°12′37"	97°36′57"	1213	102	285	0.11	19	0.26
South Central (El Reno)										
	R	Long EZ	35°33′24"	98°05′20"	1040	143	236	0.14	14	0.46
	R	Twin Otter	35°33′24"	98°05′12"	1143	183	355	0.18	14	0.46
	E	Twin Otter	35°52′16"	97°51′21"	1002	221	155	0.20	11	0.27
13 July										
North Central (Central Facility)										
	B	Twin Otter	36°11′06"	97°37′51"	1133	208	339	0.20	11	0.29
	D	Twin Otter	36°12′36"	97°36′45"	1206	194	282	0.19	11	0.31
South (Little Washita)										
	G	Long EZ	34°50′24"	97°59′51"	1220	45	274	0.06	16	0.49

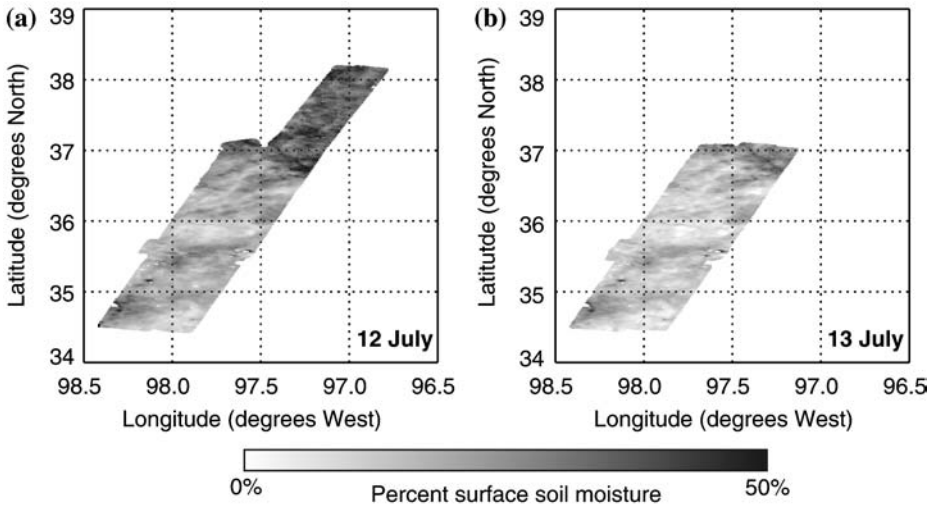

Figure 4. ESTAR derived surface soil moisture (volumetric percentage) on (a) 12 July and (b) 13 July.

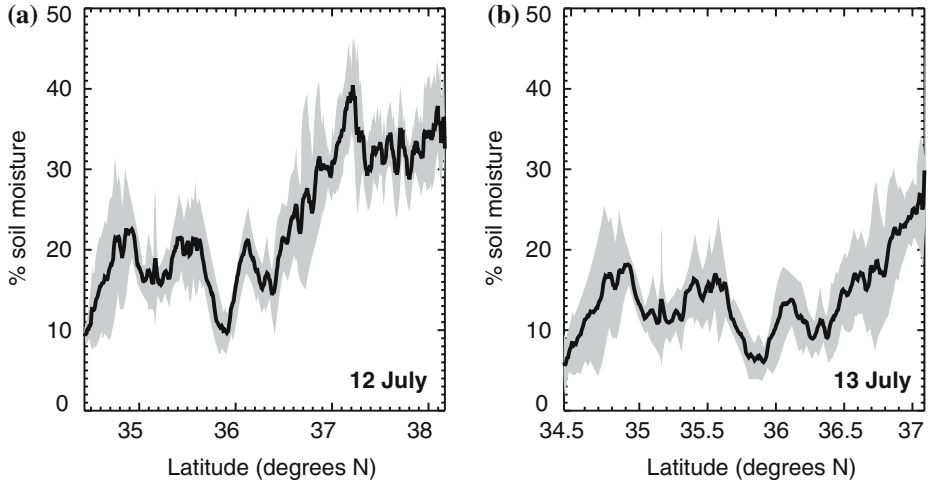

Figure 5. Mean ESTAR derived surface soil moisture from south to north averaged across all pixels from east to west for (a) 12 July and (b) 13 July. One standard deviation is shown in grey.

antecedent precipitation (Figure 2), however the secondary southern maximum (between 34.75 and 35.5° N) in soil moisture was not reflected in the precipitation gradient. The soil on average was drier on 13 July (mean 13.8% ± 9.0%) than 12 July (mean 22.2% ± 6.5%), consistent with the drying that occurred after the precipitation. No strong east–west patterns in soil moisture were observed, but observations were limited by the relatively narrow field of view for ESTAR.

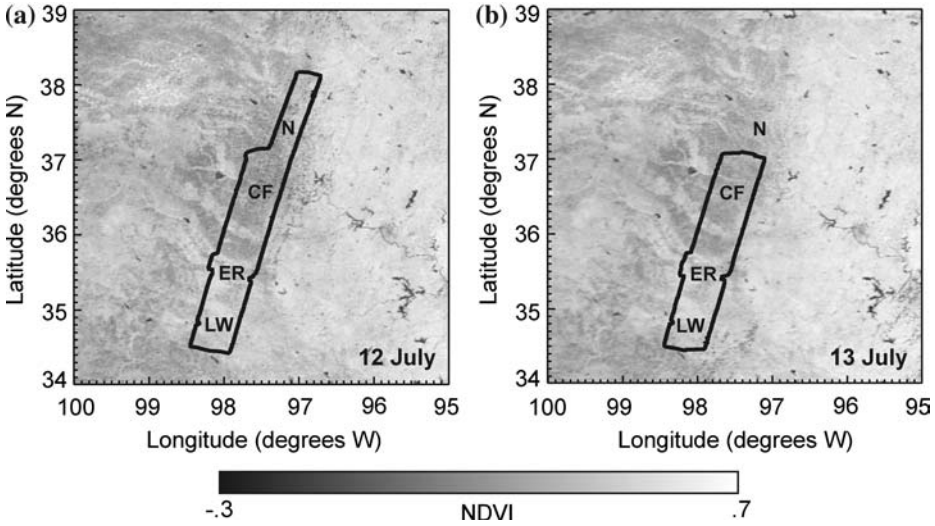

Figure 6. NOAA AVHRR NDVI for late afternoon of 12 and 13 July. An outline of the ESTAR domain is included for reference. Letters refer to regions of interest: N = northern area, CF = Central Facility area, ER = El Reno (south-central) area, LW = Little Washita (south) area.

5.3.2. *NDVI*

NDVI values revealed a large-scale pattern of increasing vegetation cover going from west to east, but no strong north–south variation (Figure 6). There were two basic regions, a western (98.5–100° W) and central (97–98.5° W) region of NDVI 0.3–0.4 and an eastern region (95–97° W) with NDVI 0.5–0.6, with a sharp change from 96.5 to 97.5° W longitude (Figure 7). Region-averaged NDVI was related to the region-averaged surface buoyancy and sensible heat fluxes, which were larger in the western and central regions compared to the eastern region, and vice versa for latent heat flux.

Unlike soil moisture or surface energy fluxes, vegetation greenness did not have any strong north–south gradients along the central part of the domain (Figure 7). NDVI was lowest (0.25–0.35) in the north central region, highest in the south central region (0.4–0.5) and moderate in the south (0.4) and the north (0.35–0.4). The gradient was the same on 12 and 13 July. These gradients were not strongly related to patterns of surface energy flux or ABL depth.

There was very little difference between mean NDVI on 12 July (0.42 ± 0.11) and 13 July (0.43 ± 0.12), which is not surprising. The slight increase in mean NDVI on 13 July occurred primarily due to an approximately 0.05 increase in NDVI among the higher NDVI pixels, whereas the areas with low NDVI remained the same. Direct comparison of ESTAR soil moisture pixels to NDVI showed no correlation.

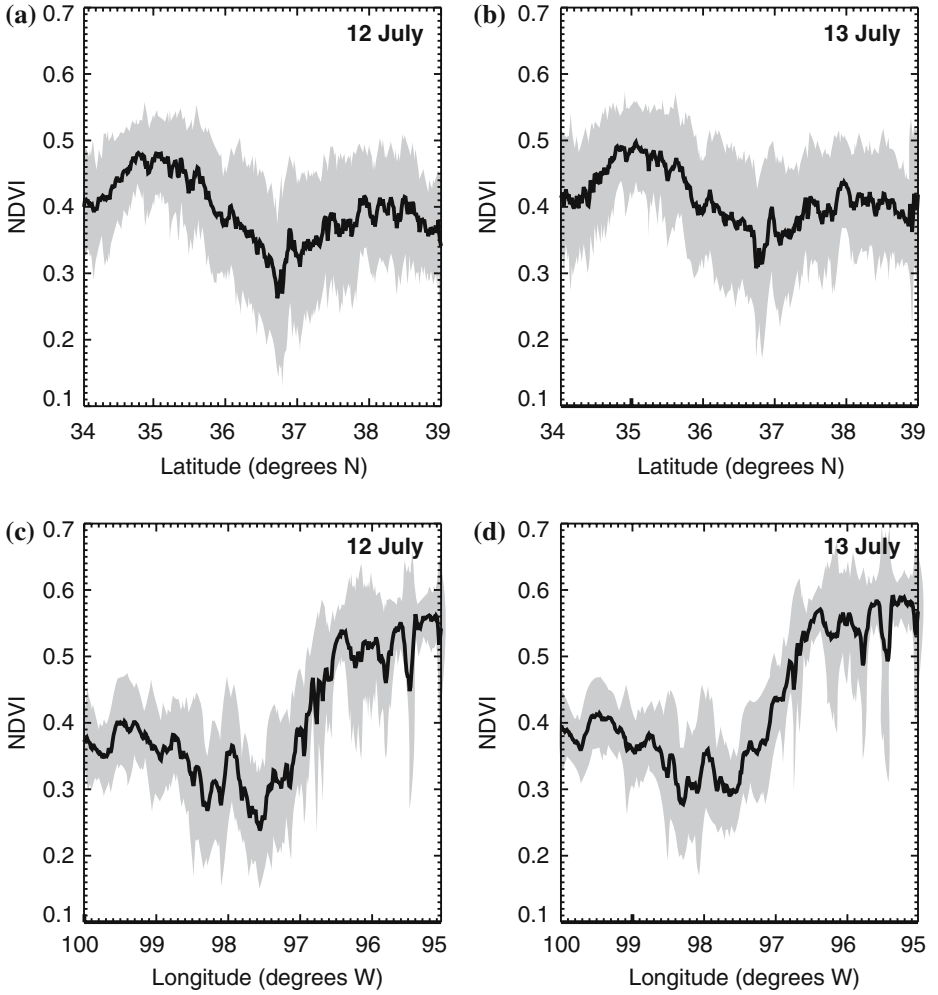

Figure 7. Mean NDVI from south to north averaged across 96.5° W to 98.5° W for (a) 12 July and (b) 13 July and mean NDVI from west to east averaged across 36° N to 37° N for (c) 12 July and (d) 13 July. One standard deviation is shown in grey.

5.3.3. *Relationship of Surface Parameters to Surface Buoyancy Flux*

No strong correlation was found between daytime NDVI and observed total integrated surface buoyancy flux from all surface stations in the SGP97 domain from 0530 to 1200 LST on 12 July ($r^2 = 0.02$) or 13 July ($r^2 = 0.05$) (Figure 8). Correlations between NDVI and sensible heat flux, latent heat flux, Bowen ratio and evaporative fraction were similarly weak (not shown). In contrast, there was a strong correlation between soil moisture and time-integrated observed surface buoyancy flux from 0530 to 1200 LST for 12 and 13 July (Figure 9). This correlation was stronger on 13 July

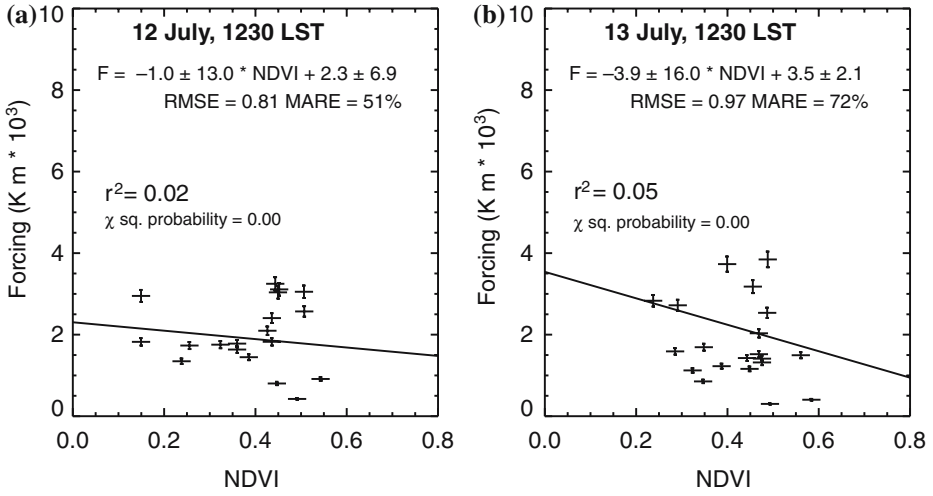

Figure 8. Correlation of NDVI to integrated buoyancy flux from 0530 to 1200 LST on (a) 12 July and (b) 13 July. Horizontal error bars represent 3×3 pixel misalignment error while vertical error bars represent a typical 10% error in turbulent flux measurements.

($r^2 = 0.80$) than 12 July ($r^2 = 0.66$). These correlations were stronger than regressions between soil moisture and mean or midday sensible heat flux, latent heat flux, Bowen ratio or evaporative fraction (not shown). Mean absolute relative error (MARE) was on average 15%, similar in range to the sum of estimated errors for soil moisture and surface fluxes. Fit slope was steeper on 13 July than 12 July, reflecting the smaller variability of soil moisture across flux towers. The difference in the slopes, however, was smaller than the uncertainty in them. Fit intercepts were similar on both days. The similarity of soil moisture to patterns of surface fluxes and ABL depth suggests that soil moisture was a major determinant of both, especially on 12 July.

Applying the linear regression and the sinusoidal model described in Equation (3), we can simulate with high correlation ($r^2 = 0.78$) and small RMSE ($0.04\,\mathrm{K\,m\,s^{-1}} \equiv 50\,\mathrm{W\,m^{-2}}$) tower-observed half-hourly surface buoyancy fluxes between 0530 and 1230 LST (Figure 10a). The model also reproduced the variations in daytime (0900–1230 LST) airplane line-average flux with high correlation ($r^2 = 0.73$), but it overestimated daytime airplane line-average buoyancy flux by an average of $0.08\,\mathrm{K\,m\,s^{-1}}$ ($100\,\mathrm{W\,m^{-2}}$) (Figure 10b). This overestimation was larger than the uncertainties in either model or airplane flux.

5.4. Modelled ABL depth

The strong correlation between surface soil moisture and time-integrated surface buoyancy flux along with the 1-D ABL model were used to model

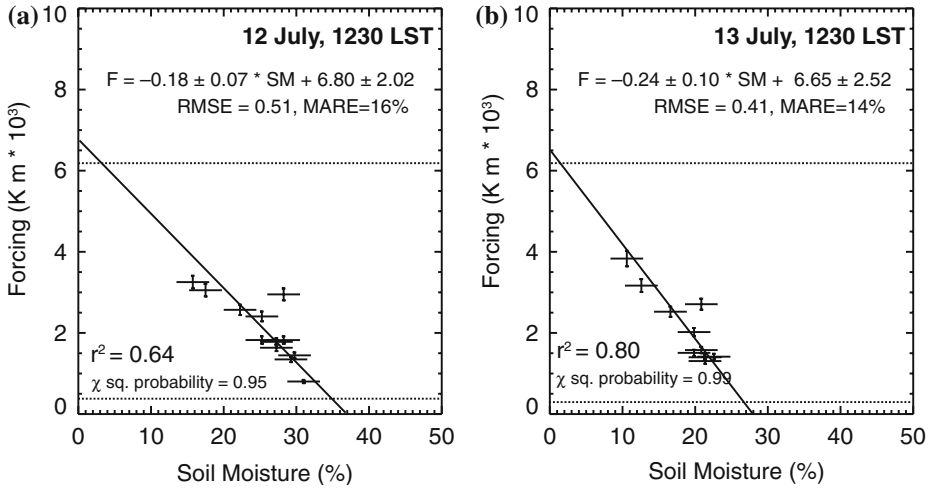

Figure 9. Correlation of ESTAR derived soil moisture to total integrated buoyancy flux from 0530 to 1200 LST on (a) 12 July and (b) 13 July. Horizontal error bars represent instrument validation error and a 3×3 pixel misalignment error while vertical error bars represent a typical 10% error in turbulent flux measurements. Dotted lines denote maximum observed time-integrated net radiative forcing and minimum observed integrated buoyancy flux, which limit the regression model extrapolated buoyancy fluxes for drier or moister than observed soil moisture.

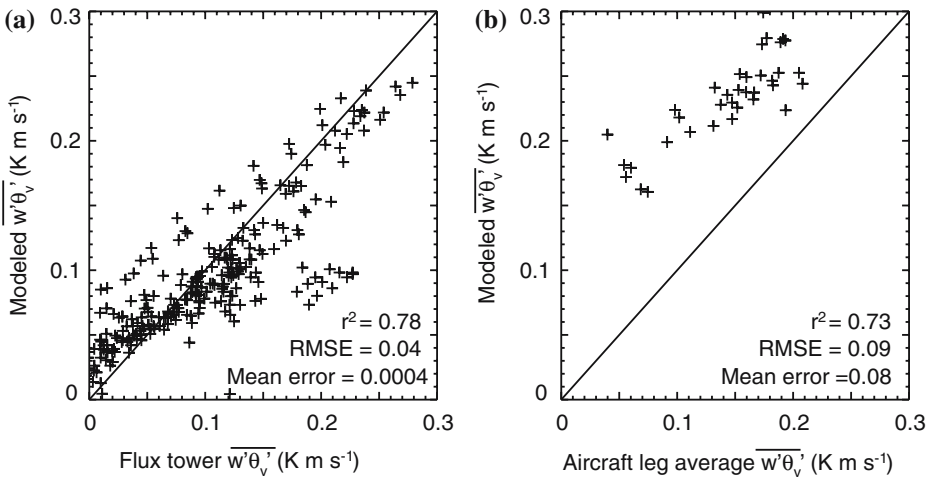

Figure 10. Relationship of modelled surface buoyancy flux to (a) half-hourly tower-observed surface buoyancy flux, and (b) leg averaged aircraft buoyancy flux on 12 and 13 July from 0530 to 1230 LST.

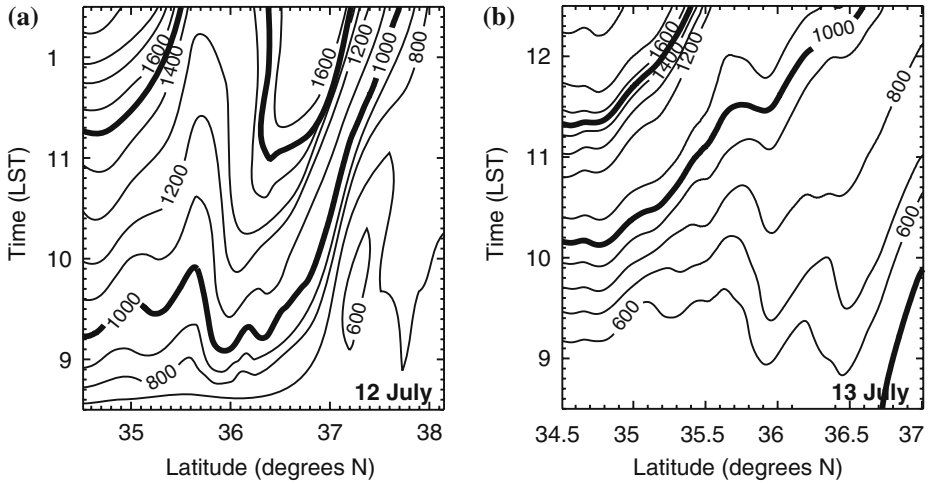

Figure 11. Modelled ABL depth (100 m contours) as a function of latitude and time for (a) 12 July and (b) 13 July.

ABL depth along the P-3 track. Model results showed ABL depth variability increasing with time as differential surface forcing allowed the ABL depth to increase faster in regions with low soil moisture compared to regions with high soil moisture (Figure 11). Spatial variations in ABL depth driven by spatial variability in both surface forcing and morning inversion strength were smoothed and shifted north by advection.

On 12 July, ABL growth was initially fastest in the north-central region while southern region depths steadily rose but quickened in growth rate after 1100 LST, in contrast to LASE observations that showed ABL growth occurring earlier in the south and later in the north central region. Consequently, the model overpredicted ABL growth in the north-central region based on central sounding results, but was better able to predict heights in regions near the northern and southern soundings (Table II). South-central ABL depth grew at the same rate as the southern region in the early morning, but then slowed down after 0930 LST. The ABL in the north had the slowest growth. By midday on 12 July, highest depths were seen in the southern and north-central regions, lowest depths in the north, and moderate depths in the south-central region, in good agreement ($r^2 = 0.45$ for 1130 LST) with LASE observations (Figure 12). By 1215 LST, modelled ABL depth variations were shifted too far north by approximately 0.5 degrees latitude, which translates to 60 km. Despite accurately reproducing variations in amplitude of ABL depth across the P-3 track, the north-central and south-central region depths were overestimated, while southern and northern region depths were well matched though underestimated at the far southern end, with an average RMSE of 375 m. Mean

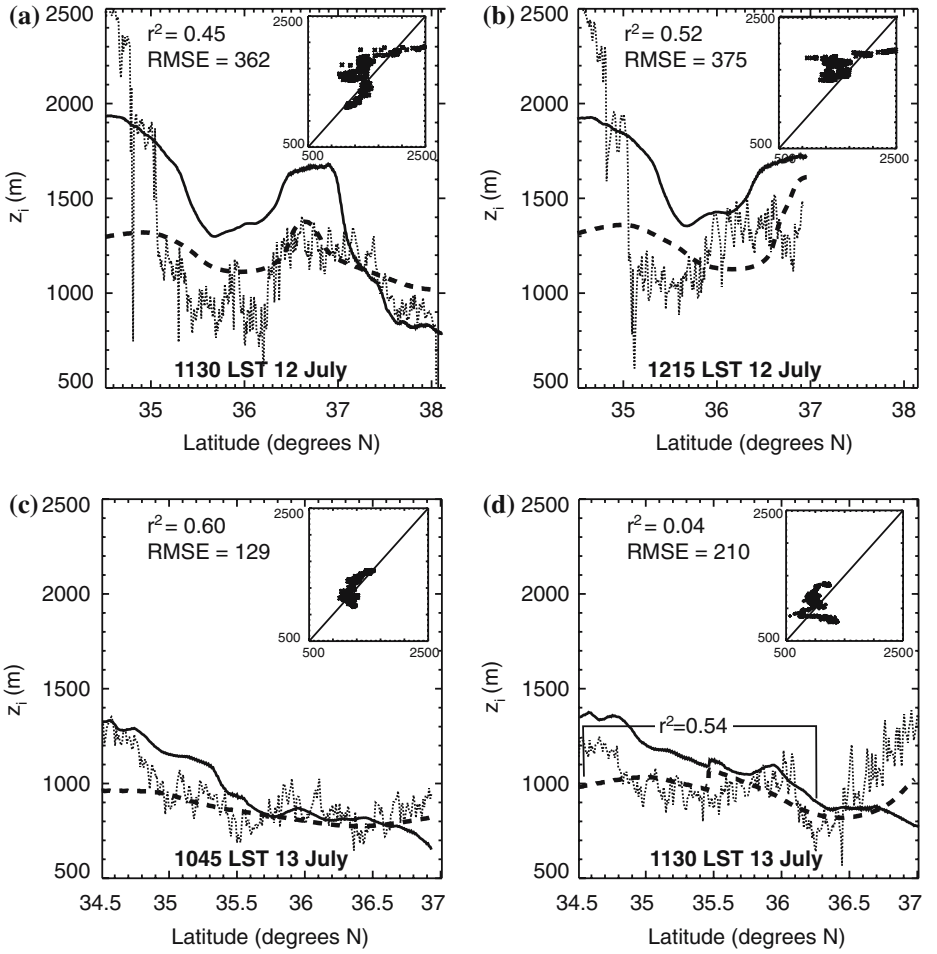

Figure 12. Comparison of LASE observed ABL depth (dotted line) to modelled ABL depth with variable surface forcing (black line) and to modelled ABL depth with constant surface forcing (dashed line) on 12 July at (a) 1130 LST and (b) 1215 LST, and on 13 July at (c) 1045 LST and (d) 1130 LST. Also shown are scatter plots of relationship of observed (*x*-axis) to modelled (*y*-axis) ABL depth with variable forcing.

model ABL depth across the whole track was 140 m larger than observed for both the 1130 and 1215 LST tracks. Midday LASE-observed ABL depth gradient from south to north ($-2.2\,\mathrm{m\,km^{-1}}$) was well predicted by the model ($-2.4\,\mathrm{m\,km^{-1}}$).

On 13 July, modelled ABL had a steadily declining ABL growth rate from south to north (Figure 11), in contrast to LASE observations, which showed little late morning growth in the southern region and fastest growth in the late morning for the northern region. Growth rates in the north-central and south-central region were similar to LASE. After midday, the

south-central region modelled ABL had rapid growth, similar to observations at the southern sounding (Table II). Midday sounding ABL depths were well reproduced by the model. Outside of the northern region, correlations to late morning and midday LASE ABL depth were higher on 13 July than 12 July (Figure 12). Mean ABL model depth was slightly higher in the model than observed by approximately 50 m and an RMSE of 170 m averaged across both tracks. On both tracks, the modelled ABL depth gradient from south to north was matched well for the late morning track ($-2.3\,\mathrm{m\,km^{-1}}$ for model, $-2.0\,\mathrm{m\,km^{-1}}$ for observed) but overestimated for midday ($-2.1\,\mathrm{m\,km^{-1}}$ for model, $-1.3\,\mathrm{m\,km^{-1}}$ for observed) outside of the northern end.

On both days, the use of ESTAR soil moisture to describe the variation in surface forcing led to a significantly improved prediction of LASE ABL depth compared to the use of constant average surface forcing along the whole track (dashed line, Figure 12). The constant forcing model underestimated mean ABL depth, and ABL depth variations were dampened. The primary exception was the northern end of the midday 1130 LST track on 13 July, where the constant forcing based model reproduced the LASE observed gradient ($7.1\,\mathrm{m\,km^{-1}}$), while the ESTAR based model had the opposite gradient ($-1.0\,\mathrm{m\,km^{-1}}$). When comparing the RMSE of observed to modelled ABL depth using coarse resolution soil moisture compared to the high resolution soil moisture case, a large jump in RMSE occurred at 64 km for 12 July and 128 km for 13 July (Figure 13), suggesting that ABL depth was primarily sensitive to soil moisture scales smaller than these values. Modelled ABL depth performed poorly at reproducing observed spatial gradient in LASE-observed ABL depth at small horizontal averaging scales and better at larger averaging scales on both days, with little change in performance above 100 km.

6. Discussion

6.1. Effect of soil moisture on surface forcing

The significant correlation between surface buoyancy flux and remotely sensed soil moisture suggests that 1-km scale average soil moisture affected surface energy fluxes measured from short towers with footprints ranging from 100s to 1000s of metres. The general gradient of wet soils to the north and more variable but dryer soils to the south, with very dry soils in the southern end and north-central region, correlated closely to the observed variability in surface buoyancy flux. Wavelet analysis revealed that SGP97 remotely sensed surface energy flux variability was dominated by variations at the 400–800 m scale, coincident with average agricultural field size

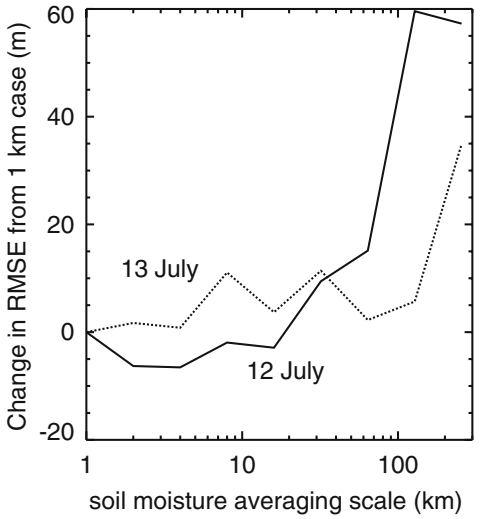

Figure 13. Difference in RMSE of observed and modelled ABL depth as a function of Soil moisture averaging horizontal length scale compared to the 1-km soil moisture case.

(Brunsell and Gillies, 2003). Analysis in one region of SGP97 showed that the impact of soil moisture on transpiration is directly proportional to variance in field-scale soil moisture and indirectly proportional to subgrid-scale soil moisture variability (Crow and Wood, 2002). Thus, the 800-m resolution of ESTAR was able to adequately resolve the dominant expected spatial variability in surface energy flux.

Soils were drier on 13 July than 12 July (Figure 4), while surface buoyancy fluxes were similar or slightly lower (Table IV), leading to a steeper slope in their relationship (Figure 9). Surface buoyancy fluxes may have been lower on 13 July due to increased plant transpiration occurring in drier, water stressed conditions just prior to stomatal closure (Wetzel and Chang, 1987). Additionally, greater variability in the sounding thermodynamic profiles and temperatures were observed on 13 July (Table II). Thus, while spatial variations in soil moisture appeared to be the primary cause of spatial variations in surface fluxes on both days, the temporal change in soil moisture is less important than changes in transpiration or atmospheric thermodynamic structure in determining day-to-day variability in surface fluxes and ABL depth.

The applicability of the surface buoyancy flux to soil moisture correlation across the SGP97 domain was dependent on how representative the surface flux stations were of all possible soil moisture conditions in the domain. The surface flux stations tended to be in areas of higher than average soil moisture for the domain. Thus, the linear correlation between surface fluxes and soil moisture for dry soils may be suspect, especially considering the overprediction of airborne fluxes (Figure 10), which generally occurred over regions

with lower line-average soil moisture than for the surface flux towers. Fortunately, most of the domain did not have very dry soil.

The sparse and low vegetation in the study area means that surface evaporation generally dominates over plant transpiration. Thus, given the sparse vegetation and 10 July rainstorm, it was not surprising that surface soil moisture availability was the main determinant of surface buoyancy fluxes on these two clear, sunny days. Bindlish et al. (2001) also showed high correlation between ESTAR soil moisture and modelled surface sensible heat fluxes from late June to mid July, but the correlation declined with increasing NDVI, especially for NDVI above 0.4. Thus, we suspect that the relationship between soil moisture and surface energy flux in the more heavily vegetated eastern region may not have been as strong.

Unlike soil moisture, the north–south pattern in NDVI did not correlate to the pattern of surface energy fluxes (Figure 8) or ABL depth, contrary to some observations in the region made over short distances by aircraft that showed stronger relationship between vegetation cover and surface energy flux (Chen et al., 2003; J. Sun, 2002, personal communication). Even though the large-scale west–east increase in NDVI was reflected in the gradient of declining surface buoyancy flux from west to east, point-by-point correlation was poor. NDVI spatial variability may have been too small to capture energy flux variability in an area with the homogeneous vegetation found in our study area. NDVI values tend to remain constant over longer time periods, corresponding to the evolution of the growing seasons and the agricultural cultivation of winter wheat. Thus, the longer term evolution of surface energy fluxes (i.e. due to changes in plant transpiration and ground cover) would be constrained by vegetation cover change, while rapid greening in the early part of the growing season can significantly affect the short-term evolution of surface energy fluxes (Chen et al., 2003). However, these effects were not important on the two days in our case study.

Our goal was not to construct a new method to remotely sense surface energy fluxes, but rather to determine what surface parameter (soil moisture or vegetation greenness) had the most influence on surface energy fluxes in our case study, and then to use that information to model the influence of the surface parameter on ABL depth. Many researchers have attempted to create and test methodologies for the measurement or calculation of surface fluxes through satellite remote sensing devices (e.g., Brutsaert et al., 1993; Pelgrum and Bastiaanssen, 1996; Chehbouni et al., 1997; Doran et al., 1998; Gao et al., 1998; Rabin et al., 2000; Ridder, 2000; Roerink and Menenti., 2000; Song and Wesely, 2003; Diak et al., 2004). These methods can be either universal (i.e. a relationship for all landscape types) or landscape-dependent (e.g. works only for grasslands), and statistically (e.g. linear correlation) or physically based (i.e. modelled

from first principles). For example, the Atmospheric Land Exchange Inversion (ALEXI) coupled soil and vegetation model (Anderson et al., 1997), which relies on remote sensing of surface temperature over multiple times in the day, sounding-derived morning thermodynamic structure and spatial information on soil and vegetation cover, has been used with some success in the Southern Great Plains region (e.g., Kustas et al., 1999; Mecikalski et al., 1999; French et al., 2000). Our results suggest that, in cases of significant antecedent precipitation spatial variability, remotely sensed surface soil moisture has a valuable role in improving model prediction or remotely sensed observations of surface energy fluxes and, in turn, estimating mesoscale ABL depth variability.

6.2. Effect of surface forcing on ABL depth

6.2.1. *Role of Initial Thermodynamic Structure*

Comparison of modelled ABL depths (Figure 11) to sounding and LASE observed ABL depths, with and without spatially variability forcing (Figure 12), suggests that soil moisture variability was the main determinant of ABL depth variability, especially on 12 July. Variability in ABL depth occurred even though all initial early morning profiles on 12 July had roughly similar increases in temperature with height in the first 1000 m, while greater variability in inversion strength was observed on 13 July (Table II). Inversion strength variability appeared to have been more important in the eastern and western regions, where strong surface forcing in the western region did not produce a large ABL depth due to a strong inversion strength, while weak surface forcing in the eastern region was able to erode a relatively weaker inversion. Inversion strength was significantly greater (from 7% to 80% larger) on 13 July than 12 July (Table II), and was a major reason that, despite drier soil moisture, the ABL depth was lower on 13 July, in addition to the larger subsidence and slightly lower surface buoyancy fluxes.

Variability in the choice of initial sounding caused average variations of 250 m across the LASE midday track, with a range of 475 m in the southern end and 130 m in the northern end, averaged over both days (Figure 14a and b). Additionally, given an arbitrary amount of forcing to any one sounding, a gradient of higher to lower potential ABL depth was observed from south to north (Figure 14c and d). These variations were smaller than the primary variations in ABL depth on 12 July, but similar to the variations on 13 July. Therefore, while surface forcing variability was the primary cause of ABL depth variability, the variation in atmospheric thermodynamic structure was of secondary importance on 12 July and of near-equal importance on 13 July.

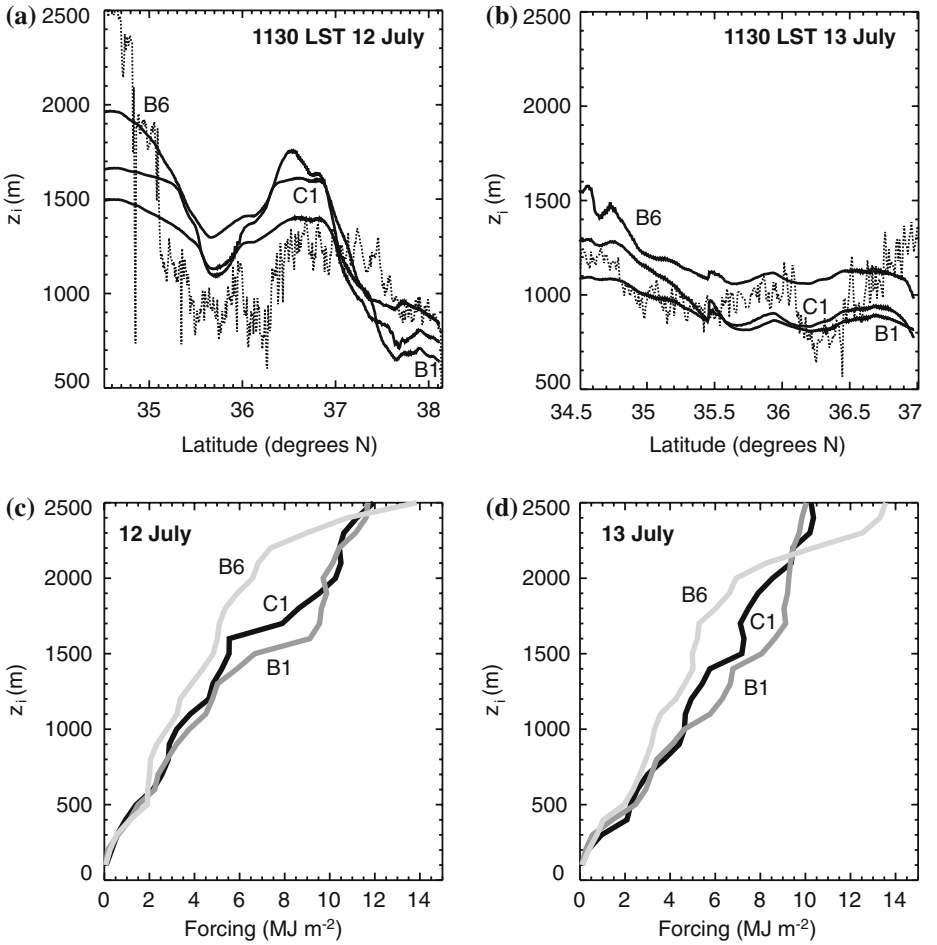

Figure 14. Effect of initial sounding choice (B1 = north, C1 = central, B6 = south) on modelled ABL depth for (a) 12 July and (b) 13 July (dotted line is observed) and potential attainable ABL depth for arbitrary amounts of total forcing for different initial early morning soundings on (c) 12 July and (d) 13 July.

The results also confirm that the initial thermodynamic structure is important in determining locations of rapid ABL growth (Findell and Elfatir, 2003). The ABL initially grows steadily as surface buoyancy and the entrainment of dry air erodes the morning inversion (Deardorff, 1980). If forcing is strong enough (due, for example, to dry soil) to realize the convective triggering potential (CTP) (Findell and Elfatir, 2003), then continued forcing leads to rapid ABL growth. The transition to rapid growth occurred in the southern part of our study area, but not in the northern part on 12 July. On 13 July, rapid growth was evident in both the southern and northern soundings, but not until later in the day. Given

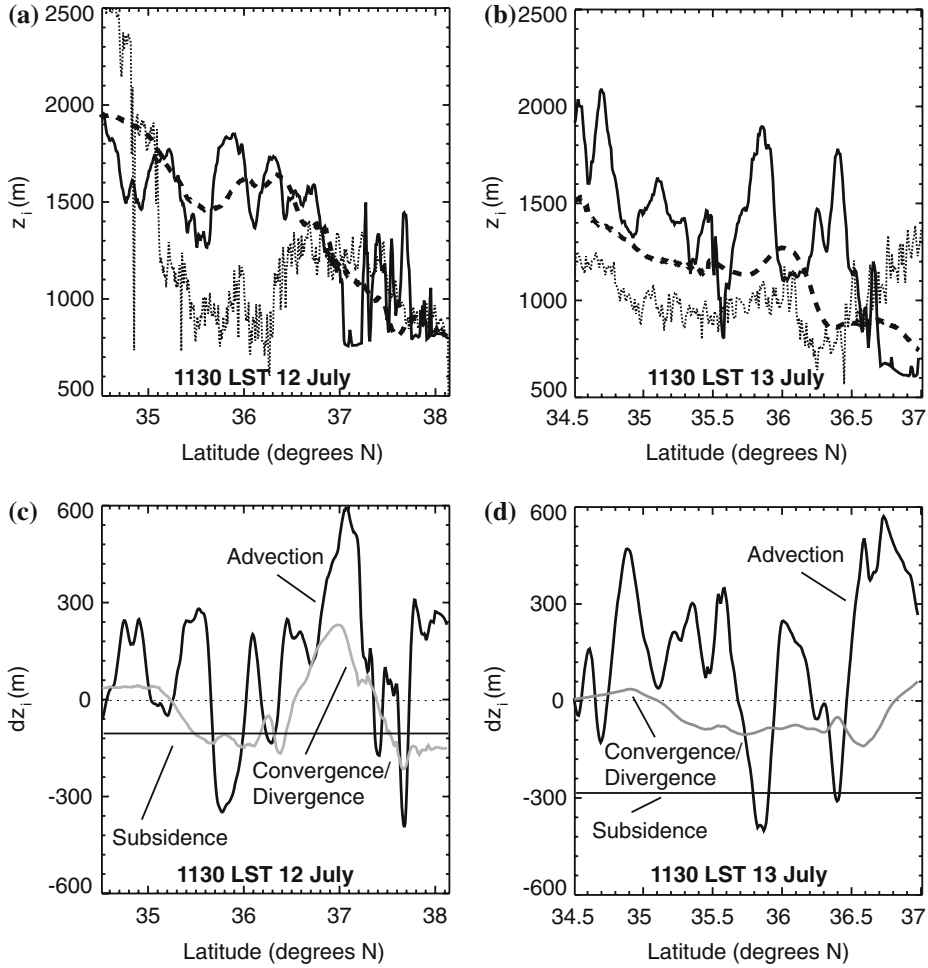

Figure 15. Modelled ABL depth with no winds (black line) and constant wind (dashed line) for (a) 12 July and (b) 13 July, and net time-integrated effect of advection (black line), convergence/divergence (grey line) and subsidence (straight line) on modelled ABL depth for (c) 12 July and (d) 13 July.

the underprediction of ABL depth by the model in the far southern end of the domain on 12 July, it may be the case that the CTP in that region was lower than the southern sounding CTP, or alternatively the entrainment flux was underestimated.

6.2.2. *Role of Advection, Convergence/Divergence, and Subsidence*

Advection, convergence/divergence and subsidence all had the impact of improving the relationship of model to observed ABL depth (Figure 15). When the model was run without these three effects, modelled ABL depth

(Figure 15a and b, solid line) was poorly correlated to observed ABL depth, with little relation between the variations in soil moisture and ABL depth except at the largest of scales (>200 km). When the model was run with variable forcing and large-scale subsidence, but a constant wind speed (Figure 15a and b, dashed line), an improvement between model and observed ABL depth was found. For 12 July, however, the constant wind speed model had poorer performance at reproducing the amplitude, location and wavelength of the observed secondary south-central minimum and north-central maximum in ABL depth than the variable wind speed model (Figure 12), suggesting that convergence/divergence of winds worked in tandem with soil moisture variations to generate ABL depth variation. In contrast, on 13 July, the constant wind speed model was better able to capture the decrease in ABL depth at 36.25° N than the variable wind speed model. Since our observations were limited to five soundings with no model dynamics, errors in sounding wind speeds and interpolation may have led to an incorrect convergence/divergence term on 13 July, which can be better captured with a 3-D mesoscale model.

Integrating each right-hand side term of Equation (5) with respect to time shows the net effect of these terms upon midday ABL depth (Figure 15c and d). Additionally, the advection term was split into an advective and convergence/divergence component:

$$\int_{t_0}^{t_1} \frac{\partial u z_i}{\partial x} = \int_{t_0}^{t_1} u \frac{\partial z_i}{\partial x} + \int_{t_0}^{t_1} z_i \frac{\partial u}{\partial x}. \tag{7}$$

The net effect of advection was to shift northward and to smooth the surface forcing. Subsidence reduced ABL depths by 100 m on 12 July and 290 m on 13 July as atmospheric pressure increased in the region. Model ABL depths on 13 July would be significantly overestimated without the subsidence term. Convergence/divergence due to changes in northward along-track wind speed on 12 July led to amplification of the secondary minimum and maximum of ABL depth that was initially set-up by the advection of variable surface forcing. With constant forcing, a secondary minimum and maximum pattern exists but the amplitude, wavelength and width are all too small (Figure 12a, dashed line). The same is true for the case of constant wind speed (Figure 15a, dashed line).

Segal and Arritt (1992) show from theoretical arguments that 50–100 km mesoscale circulations or inland breezes can occur from contrasts in surface forcing arising from soil moisture gradients. Their scaling analysis suggests that, given the wind speeds and mean forcing observed in our case study, 50-km horizontal scale variations in forcing can generate such circulations. Our scaling results showed that ABL depth responded to 50–100 km scale variations in surface forcing (Figure 13), suggesting the

possibility of secondary circulations. In Part II of our study, 3-D model simulations show that an inland breeze can be generated by the soil moisture gradient (Reen et al., submitted). The lack of a secondary maximum/minimum structure on 13 July may have been due to the increased large-scale subsidence, which has been shown in model studies to dampen surface forcing heterogeneity-induced circulations (Weaver, 2004). The lack of high-spatial density observations limits our ability to conclusively test these assertions with our simple 1-D model.

6.2.3. *Scales of ABL Depth and Surface Forcing*

Our results showed that variations in soil moisture on scales less than 64 km on 12 July and less than 128 km on 13 July were able to explain variations in ABL depth primarily for scales >100 km (Figure 13). There was poor correlation of modelled to observed ABL depth variation at small scales (<50 km), reflecting both model deficiencies and the effect of convective mixing and advection of surface heterogeneity in the ABL, as has been observed in large-eddy simulation studies (Avissar and Schmidt, 1998). Smaller scale observed variability in ABL depth was most likely a function of turbulent fluctuations.

Mahrt (2000) shows that the relationship between spatial variability in surface properties to spatial variability in ABL structure is expected to be directly proportional to the scale of surface heterogeneity and inversely proportional to wind speed, atmospheric stability and mean ABL depth. From blending height arguments, Raupach and Finnigan (1995) argue that the minimum length scale of surface heterogeneity that can influence a thermally-driven convective boundary layer is

$$L_{\min} = \frac{CUz_i}{w_*}, \tag{8}$$

where C is a constant shown to be 0.8 (Mahrt, 2000), U is the ABL wind speed, z_i is ABL depth, and w_* is the convective velocity scale:

$$w_* = \left(\frac{g}{\theta_v} z_i \left(\overline{w'\theta'_v} \right)_s \right)^{1/3}. \tag{9}$$

An alternative scaling was derived by Wood and Mason (1991) for unstable conditions where surface heating is important:

$$L_{\mathrm{wm}} = C_{\mathrm{wm}} z_i \frac{U\theta_v}{\left(\overline{w'\theta'_v} \right)_s}, \tag{10}$$

where C_{wm} is a constant shown to be 3.1×10^{-3} (Mahrt, 2000). Mahrt (2000) also notes that the largest scale of surface heterogeneity that

could significantly affect variability in ABL depth is a function of the wind speed:

$$L_{\max} = T_e U \tag{11}$$

where T_e is the entrainment time scale (Raupach and Finnigan, 1995), corresponding to the length of time available for boundary-layer growth.

These lengths scales average to 4.5 km for $L_{\min}$, 63 km for L_{wm} and 119 km for $L_{\max}$ on 12 July and 4.0 km for $L_{\min}$, 46 km for L_{wm} and 127 km for $L_{\max}$ on 13 July. Compared to our results, $L_{\min}$ appears to be too small. $L_{\min}$ and L_{wm} decreased on 13 July, but our results suggest that the length scale actually increased. It appears that, while the scale of surface heterogeneity increased on 13 July, and therefore we might have expected a stronger influence of soil moisture on ABL depth, the absolute magnitude of the spatial variation in soil moisture decreased and early morning stability increased in strength and spatial variation, leading to a decreased influence of soil moisture on ABL depth at scales smaller than 100 km, larger than both $L_{\min}$ and L_{wm}. It may also be possible that our simple 1-D model was unable to model surface heterogeneity induced variations in ABL structure at smaller scales, which a more sophisticated 3-D mesoscale model could capture.

6.2.4. *Mesoscale Modelling*

The simple 1-D model used here is unable to include the effects of 3-D advection, wind field dynamic evolution and dynamic land-surface variation on ABL depth. The model also suffers from a low data density for wind velocity. Part II explores methods for assimilating ESTAR high resolution soil moisture into the Penn State/NCAR MM5 mesoscale model for the 12 July case (Reen et al., submitted). Since a mesoscale model is able to simulate the 3-D atmospheric dynamics including convergence/divergence, mesoscale circulations, advection, entrainment, and is able to assimilate large area atmospheric and land surface boundary conditions and model dynamic changes in land-surface properties, it is expected that (1) the mesoscale model is better able to predict ABL structure than the 1-D model used here, and (2) the assimilation of high-resolution soil moisture should improve the predictions of ABL depth compared to coarser resolution observations and models. Reen et al. (submitted) demonstrate both of these effects and illustrate the reasons for some of the shortcomings exhibited by the 1-D model.

7. Conclusions

We examined land-surface forcing of ABL variability. Variations in surface buoyancy flux explained the general (>100 km) but not fine-scale mesoscale variations in ABL depth in our case study. Remotely sensed soil moisture and vegetation cover were compared at points of known surface buoyancy flux. Soil moisture was shown to be the best predictor of surface buoyancy flux variability in these two case study days following precipitation. This correlation was significantly better than the correlation between vegetation greenness and total forcing, suggesting that short term surface energy flux variability in the Southern Great Plains was driven more by soil moisture evaporation than vegetation cover. Although this result has been modelled and observed on the small scale before, the SGP97 study was a unique opportunity to observe this phenomenon on a larger scale, using a dense network of instruments along with high-resolution airborne ABL measurements.

The primary pattern of ABL development on 12 July was one of greater ABL depths in the southern end of the domain and a markedly different regime of lower ABL depths in the northern end, with a secondary minimum and maximum across the central part. The large-scale gradient was suppressed on 13 July due to changes in initial atmospheric thermodynamic conditions with space and time, an increase in subsidence, and a decline in average surface forcing. The observed north-south gradient in ABL depth matched well to the general north–south pattern of soil moisture and surface energy fluxes, but advection, convergence/divergence, subsidence and entrainment also were important determinants of ABL depth. The secondary maximum and minimum in ABL depth on 12 July appear to have been caused by variations in both wind velocity and soil moisture. The mesoscale model used in Part II provides more insight into the finer scale ABL structure and the influence of variable surface forcing upon it.

One of the goals of the Southern Great Plains 1997 study was to validate soil moisture retrieval algorithms of ESTAR for the possible future use of passive microwave remote sensing in space. While the spatial resolution (10–30 km) of a space-borne passive microwave instrument would be coarser than was available for this study (Jackson et al., 1999), it would still be useful for characterizing mesoscale surface flux and ABL depth variability. Our study showed that variations in ABL depth due to surface energy flux on fair weather days with moderate wind speeds existed on scales of 100 km, with a mesoscale model study suggesting even finer resolutions, at least for our case study. The simple model described in this paper indicates that it is possible to examine the ABL depth using remotely-sensed soil moisture and limited ground-based data at certain times and locations,

and suggests that soil moisture is an important variable to include in models of ABL development.

Acknowledgements

The authors wish to acknowledge Ronald Dobosy at NOAA Atmospheric Turbulence and Diffusion Division, J. Ian MacPherson of the National Research Council Canada, Institute for Aerospace Research, Peggy LeMone of the National Center for Atmospheric Research and an anonymous reviewer for assistance with this manuscript. The authors also wish to thank Bill Kustas, John Preuger, Tilden Meyers and Patrick Starks for use of their flux data, the Atmospheric Radiation Measurement (ARM) Program sponsored by the U.S. Department of Energy, Office of Science, Office of Biological and Environmental Research, Climate Change Research Division, and all scientists and technical staff involved in collecting data during the field campaign. This work was funded in part by grants from the U.S. National Aeronautics and Space Administration (NASA) Land Surface Hydrology Program, grant number NASA/NAG-1-193 and by the U.S. National Science Foundation (NSF), Directorate for Geosciences, Division of Atmospheric Sciences, grant number ATM-0130349.

References

Anderson, J. C., Norman, J. M., Diak, G. R., Kustas, W. P., and Mecikalski, J. R.: 1997, 'A Two-source Time Integrated Model for Estimating Surface Fluxes using Thermal Infrared Remote Sensing', *Remote Sens. Environ.* **60**, 195–216.

Avery, T. E. and Berlin, G. L.: 1992, *Fundamentals of Remote Sensing and Airphoto Interpretation*, 5th ed., Prentice-Hall, Upper Saddle River, NJ, USA, 472 pp.

Avissar, R. and Pielke, R. A.: 1989, 'A Parameterization of Heterogeneous Land-surface for Atmospheric Numerical Models and its Impact on Regional Meteorology', *Mon. Wea. Rev.* **117**, 2113–2136.

Avissar, R. and Schmidt, T.: 1998, 'An Evaluation of the Scale at which Ground-Surface Heat Flux Patchiness Affects the Convective Boundary Layer using Large-Eddy Simulations', *J. Atmos. Sci.* **55**, 2666–2689.

Batchvarova, E. and Gryning, S.-E.: 1991, 'Applied Model for the Growth of the Daytime Mixed Layer', *Boundary-Layer Meteorol.* **65**, 261–274.

Betts, A. K.: 2004, 'Understanding Hydrometeorology using Global Models', *Bull. Am. Meteorol. Soc.* **85**, 1673–1688.

Betts, A. K. and Ball, J. H.: 1996, 'The Land Surface–atmosphere Interaction: A Review based on Observations and Global Modelling Perspectives', *J. Geophys. Res.* **101(D3)**, 7209–7225.

Bindlish, R., Kustas, W. P., French, A. N., Diak, G. R., and Mecikalski, J. R.: 2001, 'Influence of Near-surface Soil Moisture on Regional Scale Heat Fluxes: Model results using Microwave Remote Sensing Data from SGP97', *IEEE T. Geosci. Remote* **39**, 1719–1728.

Browell, E. V.: 1989, 'Differential Absorption Lidar Sensing of Ozone', *P. IEEE* **77**, 419–432.

Browell, E. V. Ismail, S., Hall, W. M., Moore, A. S., Kooi, S. A., Brackett, V. G., Clayton, M. B., Barrick, J. D. W., Schmidlin, F. J., Higdon, N. S., Melfi, S. H., and Whiteman, D.: 1997, 'LASE validation experiment', in A. Ansmann, R. Neuber, P. Rairoux, and U. Wanginger (eds.), *Advances in Atmospheric Remote Sensing with Lidar*, Springer-Verlag, pp. 289–295.

Brunsell, N. A. and Gillies, R. R.: 2003, 'Length Scale Analysis of Surface Energy Fluxes derived from Remote Sensing', *J. Hydrometeorol.* **4**, 1212–1219.

Brutsaert, W., Hsu, A. Y., and Schmugge, T. J.: 1993, 'Parameterization of Surface Heat Fluxes above Forest with Satellite Thermal Sensing and Boundary-layer Soundings', *J. Appl. Meteorol.* **32**, 909–917.

Carson, D. J.: 1973 'The Development of a Dry Inversion-Capped Convectively Unstable Boundary Layer', *Qqart. J. Roy. Meteorol. Soc.* **99**, 450–467.

Chehbouni, A., Seen, D. L., Njoku, E. G., Lhomme, J. P., Monteny, B., and Kerr, Y. H.: 1997, 'Estimation of Sensible Heat Flux over Sparsely Vegetated Surfaces', *J. Hydrol.* **189**, 855–868.

Chen, F., Yates, D. N., Nagai, H., LeMone, M. A., Ikeda, K., and Grossman, R. L.: 2003, 'Land Surface Heterogeneity in the Cooperative Atmosphere Surface Exchange Study (CASES-97). Part I: Comparison of Modelled Surface Flux Maps with Surface-Flux Tower and Aircraft Measurements', *J. Hydrometeorol.* **4**, 196–218.

Crow, W. T. and Wood, E. F.: 2002, 'Impact of Soil Moisture Aggregation on Surface Energy Flux Prediction during SGP97', *Geophys. Res. Lett.* **29**, doi: 10.1029/2001GL013796.

Davis, K. J., Gamage, N., Hagelberg, C. R., Kiemle, C., Lenschow, D. H., and Sullivan, P. P.: 2000, 'An Objective Method for Determining Atmospheric Structure from Airborne Lidar Observations', *J. Atmos. Oceanic Technol.* **17**, 1455–1468.

Deardorff, J. W., Willis, G. E., and Lilly, D. K.: 1980, 'Laboratory Studies of the Entrainment Zone of a Convectively Mixed Layer', *J. Fluid Mech.* **100**, 41–64.

Diak, G. R., Mecikalski, J. R., Anderson, M. C., Norman, J. M., Kustas, W. P., Torn, R. D., and DeWolf, R. L.: 2004, 'Estimated Land Surface Energy Budgets from Space: Review and Current Efforts at the University of Wisconsin – Madison and USDA-ARS', *Bull. Am. Meteorol. Soc.* **85**, 65–78.

Dirmeyer, P. A., Zeng, F. J., Ducharne, A., Morrill, J. C., and Koster, R. D.: 2000, 'The Sensitivity of Surface Fluxes to Soil Water Content in Three Land Surface Schemes', *J. Hydrometeorol.* **1**, 121–134.

Dobosy, R. J. and MacPherson, J. I.: 1999, 'Intercomparison between Two Flux Airplanes at SGP97', in *Proceedings of the 14th Conf. on Hydrology,* Dallas, TX, January 10–15, 1999, Amer. Meteorol. Soc., 45 Beacon St., Boston, MA, pp. 137–140, preprint.

Doran, J. C., Hubbe, J. M., Liljegren, J. C., Shaw, W. J., Collatz, G. J., Cook, D. R., and Hart, R. L.: 1998, 'A Technique for Determining the Spatial and Temporal Distributions of Surface Fluxes of Heat and Moisture over the Southern Great Plains Cloud and Radiation Testbed', *J. Geophys. Res.* **103 (D6)**, 6109–6121.

Findell, K. L. and Elfatir, A. B.: 2003, 'Atmospheric Controls on Soil Moisture–Boundary Layer Interactions. Part I: Framework Development', *J. Hydrometeorol.* **4**, 552–569.

French, A. N, Schmugge, T. J., and Kustas, W. P.: 2000, 'Estimating Surface Fluxes over the SGP Site with Remotely Sensed Data', *Phys. Chem. Earth Pt. B* **25**, 167–172.

Gao, W., Coulter, R. L., Lesht, B. M., Qiu, J., and Wesely, M. L.: 1998, 'Estimated Clear-sky Regional Surface Fluxes in the Southern Great Plains Atmospheric Radiation Measurement Site with Ground Measurements and Satellite Observations', *J. Appl. Meteorol.* **37**, 5–22.

Garcia, A. L.: 2000, *Numerical Methods for Physics*, 2nd Ed., Prentice Hall, Upper Saddle River, NJ U.S.A., 423 pp.

Gillies, R. R. and Carlson, T. N.: 1995, 'Thermal Remote Sensing of Surface Soil Water Content with Partial Vegetation Cover for Incorporation into Climate Models', *J. Appl. Meteorol.* **34**, 745–756.

Gryning, S.-E. and Batchvarova, E.: 1996, 'A Model for the Height of the Internal Boundary Layer Over an Area with an Irregular Coastline', *Boundary-Layer Meteorol.* **78**, 405–413.

Hart, R. L., Cook, D. R., and Wesely, M. L.: 1998, 'The ARM Eddy Correlation System For Monitoring Surface Fluxes', in *10th Symposium On Meteorological Observations and Instrumentation*, Phoenix, AZ, 11–16 January 1998, Amer. Meteorol. Soc., 45 Beacon St., Boston, MA, pp. 335–336, preprint.

Hubbe, J. M., Doran, J. C., Liljegren, J. C., and Shaw, W. J.: 1997, 'Observations of Spatial Variations of Boundary Layer Structure over the Southern Great Plains Cloud and Radiation Testbed', *J. Appl. Meteorol.* **36**, 1221–1231.

Ismail, S., Browell, E. V., Ferrare, R. A., Senff, C., Davis, K. J., Lenschow, D. H., Kooi, S. A., Brackett, V. G., and Clayton, M. B.: 1998, 'LASE Measurements of Convective Boundary Layer Development During SGP97', in *19th Intl. Laser Radar Conf.*, Annapolis, MD, 6–10 Jaul 1998, NASA, preprint.

Jackson, T. J.: 1997, *Southern Great Plains 1997 (SGP97) Hydrology Experiment Plan*. USDA-ARS Hydrology Laboratory, Beltsville, MD U.S.A., 178 pp.

Jackson, T. J., Le Vine, D. M., Hsu, A. Y., Oldak, A., Starks, P. J., Swift, C. T., Isham, J. D., and Haken, M.: 1999, 'Soil Moisture Mapping at Regional Scales using Microwave Radiometry: the Southern Great Plains Hydrology Experiment', *IEEE T. Geosci. Remote* **37**, 2136–2151.

Koster, R. D., Dirmeyer, P. A., Guo, Z., Bonan, G., Chan, E., Cox, P., Gordon, C. T., Kanae, S., Kowalczyk, E., Lawrence, D., Liu, P., Lu, C., Malyshev, S., McAvaney, B., Mitchell, K., Mocko, D., Oki, T., Oleson, K., Pitman, A., Sud, Y. C., Taylor, C. M., Verseghy, D., Vasic, R., Xue, Y., and Yamada, T.: 2004, 'Regions of Strong Coupling between Soil Moisture and Precipitation', *Science* **305**, 1138–1140.

Kustas, W. P., Zhan, X., and Jackson, T. J.: 1999, 'Mapping Surface Energy Flux Partitioning at Large Scales with Optical and Microwave Remote-Sensing Data from Washita '92', *Water Resour. Res.* **35**, 265–277.

LeMone, M. A., Grossman, R. L., Chen, F., Ikeda, K., and Yates, D., 2003: 'Choosing the Averaging Interval for Comparison of Observed and Modelled Fluxes along Aircraft Transects over a Heterogeneous Surface', *J. Hydrometeorol.* **4,** 179–195.

Le Vine, D. M., Griffis, A. J., Swift, C. T., and Jackson, T. J., 1994: 'ESTAR: A Synthetic Aperture Microwave Radiometer for Remote Sensing Applications', *P. IEEE*, **82**: 1787–1801.

MacPherson, J. I.: 1998, *NRC Twin Otter Operations in the 1997 Southern Great Plains experiment*, National Research Council-Canada Institute for Aerospace Research. Rep. LTR-FR-146, Ottawa, Canada, 122 pp.

Mahrt, L.: 2000, 'Surface Heterogeneity and Vertical Structure of the Boundary layer', *Boundary-Layer Meteorol.* **96**, 33–62.

Mann, J. and Lenschow, D. H.: 1994, 'Errors in Airborne Flux Measurements', *J. Geophys. Res.* **99**, 14,519–14,526.

Mecikalski, J. R., Diak, G. R., Anderson, M. C., and Norman, J. M.: 1999, 'Estimating Fluxes on Continental Scales using Remote Sensed Data in an Atmospheric–Land Exchange Model', *J. Appl. Meteorol.* **38**, 1352–1369.

Pelgrum, H. and Bastiaanssen, W. G. M.: 1996, 'An Intercomparison of Techniques to Determine the Area-Averaged Latent Heat Flux from Individual In Situ Observations:

A Remote Sensing Approach using the European Field Experiment in a Desertification-Threatened Area Data', *Water Resour. Res.* **32**, 2775–2786.

Rabin, R. M., Burns, B. A., Collimore, C., Diak, G. R., and Raymond, W.: 2000, 'Relating Remotely-sensed Vegetation and Soil Moisture Indices to Surface Energy Fluxes in Vicinity of an Atmospheric Dryline', *Remote Sens. Rev.* **18**, 53–82.

Raupach, R. R. and Finnigan, J. J.: 1995, 'Scale Issues in Boundary-Layer Meteorology: Surface Energy Balances in Heterogeneous Terrain', *Hydro. Proc.* **9**, 589–612.

Ridder, K. D.: 2000, 'Remote Sensing of Parameters that Regulate Energy and Water-Transfer at the Land–Atmosphere interface', *Phys. Chem. Earth Pt. B* **25**, 159–165.

Roerink, G. J., Su, Z., and Menenti, M.: 2000, 'S-SEBI: A Simple Remote-sensing Algorithm to Estimate the Surface-Energy Balance', *Phys. Chem. Earth Pt. B* **25**, 147–157.

Segal, M. and Arritt, R. W.: 1992, 'Nonclassical Mesoscale Circulations caused by Surface Sensible Heat-Flux Gradients', *Bull. Amer. Meteorol. Soc.* **73**, 1593–1604.

Song, J. and Wesely, M. L.: 2003, 'On Comparison of Modelled Surface Flux Variations to Aircraft Observations', *Agr. Forest Meteorol.* **117**, 159–171.

Tennekes, H.: 1973, 'A Model for the Dynamics of the Inversion above a Convective Boundary layer', *J. Atmos. Sci.* **30**, 558–567.

Twine, T. E., Kustas, W. P., Norman, J. M., Cook, D. R., Houser, P. R., Meyers, T. P., Prueger, J. H., Starks, P. J., and Wesely, M. L.: 2000, 'Correcting Eddy-Covariance Flux Underestimates over a Grassland', *Agr. Forest Meteorol.* **103**, 279–300.

Weaver, C. P.: 2004, 'Coupling between Large-scale Atmospheric Processes and Mesoscale Land–Atmosphere Interactions in the U.S. Southern Great Plains during Summer. Part I: Case Studies', *J Hydrometeorol.* **5**, 1223–1246.

Wesely, M. W., Cook, D. R., and Coulter, R. L.: 1995, 'Surface Heat Flux Data from Energy Balance Bowen Ratio Systems', in *Ninth Symposium on Meteorological Observations and Instrumentation*, Charlotte, NC, 27–31 March 1995, Amer. Meteorol. Soc., 45 Beacon St., Boston, MA, pp. 486–489, preprint.

Wetzel, P.J. and Chang, J.: 1987, 'Concerning the Relationship between Evapotranspiration and Soil Moisture', *J. Clim. Appl. Meteorol.* **26**, 18–27.

Wood, N. and Mason, P. J.: 1991, 'The Influence of Stability on the Effective Roughness Lengths for Momentum and Heat Flux', *Quart J. Roy. Meteorol. Soc.* **117**, 1025–1056.

Yan, H. and Anthes, R. A.: 1988, 'The Effects of Variations in Surface Moisture on Mesoscale Circulations', *Mon. Wea. Rev.* **116**, 192–208.

Zhong, S. and Doran, J. C.: 1997, 'A Study of the Effects of Spatially Varying Fluxes on Cloud Formation and Boundary Layer Properties using Data from the Southern Great Plains Cloud and Radiation Testbed', *J. Climate* **10**, 327–341.